Introducing a Critical Droplet Radius for Coalescence in Turbulent Emulsions

van Aartsen, Stijn C.

Award date:
2021

EINDHOVEN UNIVERSITY OF TECHNOLOGY

Department of Applied Physics
Fluids and Flows Group

Introducing a Critical Droplet Radius for Coalescence in Turbulent Emulsions

Master Thesis

S.C. van Aartsen
Student ID: 1504878

Supervisor:
Prof. dr. F. Toschi

External Committee Members:
Prof. dr. A.A. Darhuber
Prof. dr. ir. P.D. Anderson

R-2090-A

This thesis is the final report of a 45 EC Graduation Project of the Master Applied Physics, track Transport Physics. The TU/e Code of Scientific Integrity is followed.

Eindhoven, October 2021

Abstract

Emulsions are highly interesting systems in both physics and chemistry with many applications for example in the food industry. Understanding the physics of emulsions is complicated since many fluid parameters like surface tension and viscosity of both fluids play a role. This study explores the implications on droplet size of introducing a disjoining pressure in turbulent emulsions.

The classical Hinze argument states that the maximum droplet size in turbulent emulsions scales as $\varepsilon^{-2/5}$ with ε the energy dissipation rate. For low mass fractions this scaling has been verified experimentally. The argument from Hinze is solely based on droplet breakup in emulsions, in absence of a disjoining pressure. The presence of a disjoining pressure influences the process of droplet coalescence, thereby affecting the droplet size. We start by considering binary droplet coalescence, and propose a mere phenomenological argument equivalent to the one of Hinze, resulting in a critical droplet radius for coalescence scaling as $\varepsilon^{-1/4}$.

Using Lattice Boltzmann simulations, the proposed argument for critical binary droplet coalescence is verified. Our validation was limited to rather the idealised two-dimensional droplet coalescence events. In three-dimensional turbulent emulsions, we expect the phenomenology to be more complex. Therefore, the prediction of the critical radius in turbulence has not been verified, and how this radius competes with the Hinze radius is still to be explored. Numerical simulation of complete turbulent emulsions thereby investigating the critical droplet radius for coalescence is subject for further research.

Contents

Chapter 1

Introduction

Opposed to laminar flow, turbulent flow is far more complicated. Although the exact flow patterns cannot be calculated since it highly depends on initial conditions, a statistical theory can be derived.[8] Kolmogorov presented theories which are considered classical today about the energy cascade and turbulence length scales[16]. The theoretical framework made it possible to apply the laws of turbulence to both small and large length scales.

Having two immiscible fluid phases makes the turbulence more complex, but gives rise to additional interesting physics. For example the fluid interface is susceptible to instability when a shear is applied: the Kelvin-Helmholtz instability. This instability is visible at a flat interface between two fully separated fluids. However, such a flat interface is not always present. Emulsions for example are a whole different class of multi-fluid systems. In an emulsion small droplets of a fluid are dispersed in an immiscible fluid. This implies another length scale is introduced: the droplet size of the emulsified phase.

One of the earliest theoretical work on turbulence in emulsions is by Hinze who proposed the scaling of maximum droplet diameter turbulence intensity[13], which is verified experimentally for low volume fraction emulsions both by experiments[28] and numerical simulations[22]. Following his work, more precise descriptions of droplet size have been reported, e.g. with the introduction of the inertial and viscous subranges[5]. The interest in emulsions in turbulence is clear since it has a wide range of applications, from food processing[20] to oil refinery[27].

From the insights on microscopic droplet level, theories and models have been developed for describing macroscopic characteristics of emulsions. Among the macroscopic properties are the effective viscosity of the emulsion. The effective viscosity of oil-in-water emulsions is found to increase with volume fraction and can be described by the Herschel-Bulkley model for its shear-thinning properties[28].

Increasing the volume fraction in an emulsion comes with more interesting physics, since the droplets cannot be considered isolated. Phase inversion can occur, where the emulsified phase becomes the continuous phase and vice versa. It had been shown that phase inversion can be induced by e.g. temperature changes and addition of surfactants.[17].

A theoretical model by Ostwald stated that the maximum volume fraction of the emulsified phase is the volume fraction of a close-packing of spheres[17]. The limitations are clear since equally sized spherical droplets are assumed and any droplet-droplet interactions or stirring is not accounted for, so in practice the maximum volume fraction of the emulsified phase should not be

able to be exceed 50%. However, in practice it is easily possible to achieve higher volume fraction, of which mayonnaise is a famous example[11].

The reason why high volume fractions can be achieved, is the presence of a disjoining pressure between the droplets. In general, this disjoining pressure is caused by the presence of surfactants at the fluid-fluid interface. By various mechanisms, these surfactants repel other interfaces in close proximity preventing them to get in contact and merge. It has been shown that in general the disjoining pressure increases with increasing surfactant concentration, up to the saturation concentration[14]. A strong effect of surfactants can withstand large droplet deformations, preventing droplets to relax to their spherical equilibrium shape. This so-called jamming of droplets in an emulsion can give rise to a finite yield stress[23] in the emulsion, which is found to be dependent on the droplet radius and interfacial tension. Besides those two, there are other relevant factors, for example the polydispersity of droplet size and homogeneity of the droplet distribution.

We see that disjoining pressure plays an important role in understanding the physics of emulsions in general and in turbulent flow in particular. However, models predicting droplet size distributions (e.g. the Hinze scaling) are based on the process of droplet breakup. Although this is the major process accounting for the physics found in emulsions in many cases, in some cases the repulsion between droplets may play a significant role. From the stabilised emulsions we know that disjoining pressure has a major effect in emulsions with high volume fraction. However, if the disjoining pressure is strong enough, it also plays a role for emulsions with intermediate or low volume fractions (classically the regime where the Hinze scaling is valid). This implies a more sophisticated model is required that includes not only the mechanism of droplet breakup but also of droplet coalescence. In this work a model equivalent to Hinze is provided, for droplet coalescence. Using both this novel model and the known Hinze theory can give deeper insight in the droplet radius distribution found in emulsions. In order to come to this model, this work start by investigating the effect of disjoining pressure on the coalescence of droplets in a (turbulent) flow.

Chapter 2

Physics of emulsions

All Newtonian fluid flows are governed by the most important equation in fluid mechanics, the Navier-Stokes (NS) equations:

$$\frac{\partial \boldsymbol{u}}{\partial t} + (\boldsymbol{u} \cdot \nabla)\boldsymbol{u} - \nu \boldsymbol{\nabla}^2 \boldsymbol{u} = -\frac{1}{\rho}\boldsymbol{\nabla} p + \boldsymbol{F} \tag{2.1}$$

$$\boldsymbol{\nabla} \cdot \boldsymbol{u} = 0 \tag{2.2}$$

Equations (2.1) and (2.2) are the Navier-Stokes Equations for incompressible flow, with the terms from left to right: change of the flow field, advection, viscous forces, pressure and an external body force such as gravity. For simple cases, the NS-equation has analytical solutions. For example for a shear flow, in absence of gravity or pressure gradients, induced by a moving wall with no-slip boundary conditions, all terms except for the viscous forces are zero. Although shear flow is an extremely simple case, also for other cases of laminar flow (e.g. pressure driven pipe flow) analytical solutions can be derived.

However, if the Reynolds number, defined as $Re = UL/\nu$, is high, the flow is generally not steady (i.e. the first term in the NS-equation is nonzero) and the flow becomes turbulent. In the definition of the Reynolds number, U is the characteristic flow speed, L is the characteristic length scale and ν is the kinematic viscosity. Turbulent flows are chaotic, shifting the description from the deterministic prediction the exact flow pattern to a statistical approach. In 1922 Richardson proposed the concept of the energy cascade. This model states that energy input takes place at the macroscopic scale, after which it cascades down to smaller length scales and finally dissipates due to viscosity. Following Richardson's work, Kolmogorov developed theories on isotropic turbulence. One of his famous results is the characteristic length scale for energy dissipation[16]:

$$\lambda = \left(\frac{\nu^3}{\varepsilon}\right)^{1/4} \tag{2.3}$$

in which ε is the viscous energy dissipation. In the same manner, a characteristic time scale and velocity scale can be obtained:

$$\tau = \left(\frac{\nu}{\varepsilon}\right)^{1/2} \tag{2.4}$$

$$u = (\nu\varepsilon)^{1/4} \tag{2.5}$$

Well above the length scale λ and well below the macroscopic length scale L, is the inertial range[25]: $\lambda \ll l \ll L$, for which Kolmogorov introduced his two-thirds law:

$$\delta v(l)^2 \sim \varepsilon^{2/3} l^{2/3} \tag{2.6}$$

which state that a variation in fluid velocity over a distance l scales in this specific manner, given l is within the inertial range where energy dissipation is negligible. Kolmogorov and others have developed more sophisticated models on (isotropic) turbulence (e.g. [15]), investigating the dependency of energy on wavenumber. The interested reader is encouraged to read further on this topic, e.g. starting with a review in ref [25]. However, it is not further discussed here since it is of minor relevance to the current work.

What is relevant to this work, is how the dependency on length scale relates to the droplet length scale in emulsions, the latter being the droplet radius, R. Breakup and coalescence are two highly relevant phenomena found in emulsions. Below we show how droplet breakup is governed by equation (2.6) via the Hinze relation. Droplet coalescence is the subject of the rest of this report.

2.1 Hinze relation

Droplet breakup in turbulent emulsions is described by the Hinze relation[13]. This relation is derived starting from the criterion for droplet breakup in turbulence, given by $We \sim 1$, where:

$$We = \frac{\rho v^2 R}{\sigma} \sim \frac{E_{kin}}{E_{surf}} \tag{2.7}$$

The condition $We \gg 1$ indicates that the kinetic energy available over the droplet volume is large enough to overcome the energy barrier of creating additional surface area.

For completeness, we also provide the breakup criterion in case of laminar flow. Then the breakup criterion takes the form of the Capillary number:

$$Ca = \frac{\rho\nu v}{\sigma} = \frac{\rho\nu\dot{\gamma}R}{\sigma} \sim 1 \tag{2.8}$$

With $\dot{\gamma}$ being the shear rate. However, for now we only focus on breakup governed by the Weber number in order to derive the classic Hinze relation which predicts the critical breakup radius is turbulence. For the velocity we use the velocity variance over a distance R which we calculate using equation (2.6). Filling in equation (2.7) gives:

$$\frac{\rho\varepsilon^{2/3}R^{2/3}R}{\sigma} \sim 1 \tag{2.9}$$

Rewriting gives the familiar Hinze scaling:

$$R_{crit} \sim \left(\frac{\sigma}{\rho}\right)^{3/5} \varepsilon^{-2/5} \tag{2.10}$$

Equation (2.6) can also be applied to the integral length scale L instead of the droplet radius R:

$$v_{rms}^2 \sim \varepsilon^{2/3} L^{2/3} \tag{2.11}$$

with v_{rms} being the root mean square velocity. This allows writing ε in terms of the Reynolds number $Re = \frac{L v_{rms}}{\nu}$. After some rewriting:

$$\varepsilon \sim \frac{Re^3 \, \nu^3}{L^4} \tag{2.12}$$

In conclusion, the critical droplet radius R_{crit} can be written in terms of the Reynolds number by substituting ε, to obtain:

$$R_{crit} \sim \left(\frac{\sigma}{\rho}\right)^{3/5} \nu^{-6/5} L^{8/5} \, Re^{-6/5} \tag{2.13}$$

Thus in homogeneous turbulent flow, the critical radius for droplet breakup scales as $Re^{-1.2}$.

2.2 Disjoining pressure

The disjoining pressure Π for interfaces separated by a distance d can be defined as[3]:

$$\Pi(d) = P_N - P_B \tag{2.14}$$

with P_N the normal force per unit area on the interface and P_B the bulk pressure of the liquid between the interfaces. In other words, the disjoining pressure is a pressure which can originate from anything except for simple hydrodynamical pressure. Among many others, the most important origins for disjoining pressure are (electric double-layer) electrostatic forces, Van der Waals forces and steric hindrance of surfactants[26]. The most used method to measure disjoining pressure is thin-film pressure balance (TFPB)[26]. In this method a thin liquid film is formed in a surrounding gas with variable pressure. From the balance between the gas pressure, fixed internal pressure in the liquid and Laplace pressure the disjoining pressure can be calculated. The film thickness is measured by interferometry. An other method that can be used is pushing an oil droplet towards an oil-water interface[2]. Using this technique, a water film thickness up to 5 nm could be achieved, measuring a disjoining pressure in the range 50 - 2000 Pa. A film thickness down to several nanometers is required since the disjoining pressure is also in the nanometer range, due to its molecular origin.

2.3 Droplet coalescence

Now that the concept of disjoining pressure has been introduced, it is important to investigate how droplets coalesce. In the classical Hinze scaling for example, it is assumed that droplets coalesce immediately in case the interfaces touch. However, this cannot be assumed anymore in case of significant disjoining pressure.

A disjoining pressure prevents two interfaces from coming close, as illustrated by figure 2.1. The schematic graph shows that the strength of the disjoining pressure sharply decreases with separation distance and that a critical value d_{crit} exists below which the disjoining pressure cannot withstand the attractive force from the interface and the two droplets coalesce. Feng[9] investigated

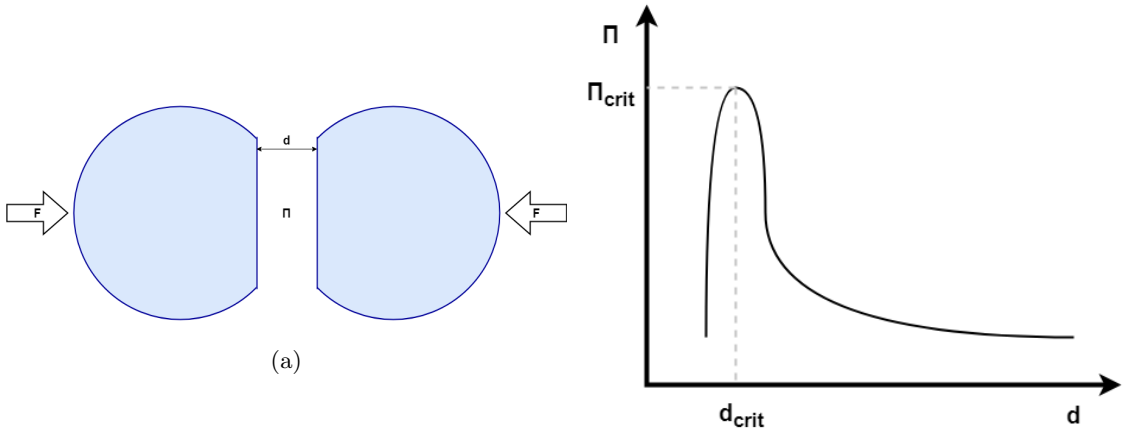

Figure 2.1: (a) Schematic figure of disjoining pressure preventing two droplet interface from coming in close proximity withstanding an external force. (b) Sketch of the dependency of Π on separation distance d. Figures inspired by Feng[9].

the critical distance d_{crit} and associated Π_{crit} by drying dense emulsions causing the fluid layer in between to become thinner.

In this case, the droplets carry no momentum, since the initial condition is a stabilised emulsion and the film thickness decreases slowly. Yoon et al.[29] performed simulations of binary droplet coalescence. Two droplets collide, after which they coalesce. A fixed value for the disjoining pressure was used and the time before coalescence occurred was measured. The following result was found:

$$t\dot{\gamma} \sim Ca \tag{2.15}$$

for low Capillary number and

$$t\dot{\gamma} \sim Ca^{4/3} \tag{2.16}$$

for high Capillary number. $\dot{\gamma}$ is the strain rate, which implies $t\dot{\gamma}$ is a dimensionless time. Note that $\dot{\gamma}$ is present in the expression for the Capillary number, equation (2.8). The reason for the two distinct scalings is that the droplets remain spherical in case of low Capillary number and deform in case of high Capillary number.

For further investigation of binary droplet coalescence, we introduce all energies that play a role, being the kinetic energy E_{kin}, surface energy E_{surf} and repulsion energy E_{rep}:

$$E_{kin} = 0.5\rho V v^2 \tag{2.17}$$

$$E_{surf} = \sigma A \tag{2.18}$$

$$E_{rep} = \int_0^\infty F_{rep} dh = \int_0^\infty \int_A \Pi(h) dS dh \tag{2.19}$$

Equation (2.19) is the integral of the curve in figure 2.1, integrated over the droplet surface, yielding the energy barrier to overcome for two droplets to coalesce. Conservation of energy dictates:

$$E_{kin}(t) + E_{surf}(t) + E_{rep}(t) + E_{diss}(t) = constant \tag{2.20}$$

where $E_{diss}(t)$ is the energy dissipated between time $t = 0$ and time t.
Lastly, we provide the definition of the Laplace pressure:

$$\Delta P = \frac{2\sigma}{R} \tag{2.21}$$

with ΔP the pressure drop over an interface of a droplet with radius R.

Chapter 3

Numerical methods

In this section, we first introduce the numerical method that is used to model binary droplet coalescence: the Lattice Boltzmann Method (LBM). Hereafter, the setup for the droplet collision simulations is described including how to obtain all relevant data.

3.1 Lattice Boltzmann Method

The Lattice Boltzmann Equation (LBE) can simply be viewed as a discretisation of the Boltzmann Equation (BE), i.e. literally the Boltzmann Equation discretised on a (square) lattice. First, we introduce the BE, which uses a distribution function $f(\boldsymbol{x}, \boldsymbol{v}, t)$ which is a function of position, velocity and time and corresponds to the chance that a "gas" particle is found in that part of the phase space. The function f contains all information on the fluid state, implying all fluid parameters can be derived from it[10]. The two most important and fundamental ones being the fluid density and momentum:

$$\rho(\boldsymbol{x}, t) = \int f(\boldsymbol{x}, \boldsymbol{v}, t) d\boldsymbol{v} \tag{3.1}$$

$$\rho(\boldsymbol{x}, t)\boldsymbol{u} = \int f(\boldsymbol{x}, \boldsymbol{v}, t)\boldsymbol{v} d\boldsymbol{v} \tag{3.2}$$

Using equations (3.1) and (3.2) other quantities such as fluid velocity, kinetic energy and stress tensor can be derived. For example, the fluid velocity is obtained by dividing the momentum by the density.

Knowing how to derive properties from f, it is important to have an expression for calculating f itself. Or, more precisely, an expression for $\frac{\partial f}{\partial t}$ so that the evolution of f is known, starting from an initial condition f_0. Actually, $\frac{\partial f}{\partial t}$ consists of three independent contributions: diffusion $\left(\frac{\partial f}{\partial t}\right)_{diffusion}$, (external) forcing $\left(\frac{\partial f}{\partial t}\right)_{force}$ and collisions between fluid particles $\left(\frac{\partial f}{\partial t}\right)_{collision}$. Including expressions for all three contributions yields [10]:

$$\frac{\partial f}{\partial t} + \boldsymbol{v} \cdot \boldsymbol{\nabla}_x f + \boldsymbol{a} \cdot \boldsymbol{\nabla}_v f = \Omega(f) \tag{3.3}$$

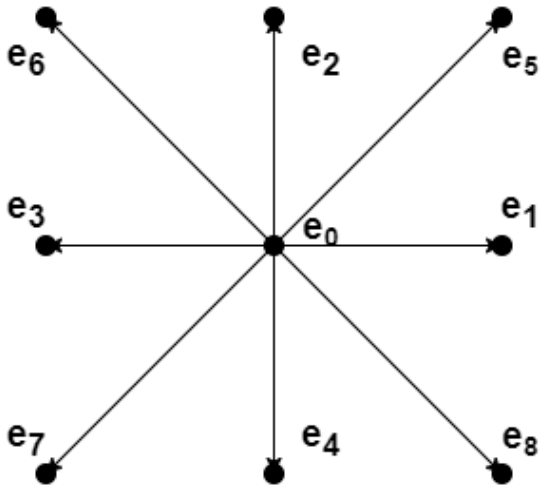

Figure 3.1: Visualisation of the D2Q9 model, where nine velocities are possible, labeled $\boldsymbol{e}_i$ with $i = 0, ..., 8$.

In equation (3.3) we recognise all terms. On the left hand side: overall evolution of f, diffusion and forcing, where $\boldsymbol{a} = \boldsymbol{F}/m$ is the acceleration. $\Omega(f)$ is a yet unknown expression accounting for collisions. Solving equation (3.3) comes with the freedom for choosing an expression for Ω, attempting to maximise both the accuracy of the physical description and stability of the numerical scheme used. A widely used expression for Ω, which is also used in this work, is the Bhatnagar Gross and Krook (BGK) approximation[4]. Bhatnagar, Gross and Krook proposed that particle collision cause the distribution function f to relax to equilibrium, i.e. f^{eq}, in a characteristic time, τ, being a free parameter:

$$\left(\frac{\partial f}{\partial t}\right)_{collision} = \Omega(f) = -\frac{1}{\tau}(f - f^{eq}) \tag{3.4}$$

where f^{eq} is assumed to be the Maxwell-Boltzmann distribution:

$$f^{eq}(\boldsymbol{x}, \boldsymbol{v}, t) = \rho(\boldsymbol{x}, t)\left(\frac{m}{2\pi k_B T}\right)^{3/2} e^{-\frac{mv^2}{2k_B T}} \tag{3.5}$$

In equation (3.5): $v \equiv |\boldsymbol{v} - \boldsymbol{u}(\boldsymbol{x}, t)|$ where $\boldsymbol{u}(\boldsymbol{x}, t)$ is the velocity that could be calculated using equations (3.1) and (3.2).

The next step is to build the numerical scheme from the Boltzmann Equation (3.3) to yield the LBE. Space, velocity and time are all discretised, by convention single steps in both space and time are given both unit value: $\Delta x = 1$ and $\Delta t = 1$. Setting these two values restricts the possible values for velocity. The set of velocities used is indicated by DdQq, where d is the number of dimensions and q the number of discrete velocities. Commonly $d = 2$ or $d = 3$, and some common sets are D2Q9, D3Q15, D3Q19 and D3Q27. Figure 3.1 shows a visualisation of all nine allowed velocities in D2Q9.

For e.g. D2Q9 or D3Q27, the physical velocity in lattice direction is fundamentally limited to $v_{max} = \frac{\Delta x}{\Delta t}$ with the important note that actual velocities should be well below this upper bound for accurate and stable results. Including more discrete velocities increases both this upper bound and stability, at the cost of computation time.

Discretising equations (3.3) and (3.4) gives[1]:

$$f_i(\boldsymbol{x} + \boldsymbol{e}_i\Delta t, t + \Delta t) - f_i(\boldsymbol{x}, t) = \Omega(f_i) \tag{3.6}$$

$$f_i(\boldsymbol{x} + \boldsymbol{e}_i\Delta t, t + \Delta t) - f_i(\boldsymbol{x}, t) = -\frac{1}{\tau}\left(f_i(\boldsymbol{x}, t) - f_i^{eq}(\boldsymbol{x}, t)\right) \tag{3.7}$$

As before $i = 0...q-1$ indicates one of the possible velocities.

The collision term $\Omega(f_i)$ has to satisfy both mass and momentum conservation:

$$\sum_i \Omega(f_i) = 0 \tag{3.8}$$

$$\sum_i \Omega(f_i)\boldsymbol{e}_i = \boldsymbol{0} \tag{3.9}$$

Every timestep in an LBM consists of three essential steps, being calculation of fluid quantities, collisions and streaming.

First, fluid density and momentum are calculated by the discretised versions of equations (3.1) and (3.2):

$$\rho = \sum_i f_i \tag{3.10}$$

$$\rho\boldsymbol{u} = \sum_i f_i\boldsymbol{e_i} \tag{3.11}$$

Secondly, collisions are taken into account by calculating the distribution functions after collision:

$$\tilde{f}_i(\boldsymbol{x}, t) = f_i(\boldsymbol{x}, t) - \frac{1}{\tau}\left(f_i(\boldsymbol{x}, t) - f_i^{eq}(\boldsymbol{x}, t)\right) \tag{3.12}$$

Here, f_i^{eq} is calculated using a discretised approximation of Maxwell-Boltzmann distribution (equation (3.5))[24][6]:

$$f_i^{eq} = \rho w_i\left(1 + \frac{\boldsymbol{e}_i \cdot \boldsymbol{u}}{c_s^2} + \frac{(\boldsymbol{e}_i \cdot \boldsymbol{u})^2}{2c_s^4} - \frac{\boldsymbol{u}^2}{2c_s^2}\right) \tag{3.13}$$

c_s is the speed of sound which is equal to $1/\sqrt{3}$. w_i are relative weights associated with the discrete velocities, being $w_0 = 4/9$, $w_1 = w_3 = w_5 = w_7 = 1/9$ and $w_2 = w_4 = w_6 = w_8 = 1/36$ in D2Q9. Furthermore, the value for τ used in equation (3.12) is related to the kinetic viscosity via $\nu = (2\tau - 1)/6$. In practice, for the BGK approximation, $\tau = 0.55$ appears to be the lower bound and this value is used for all numerical simulations presented in this work.

Lastly, the streaming step is performed, where the fluid particles stream along their discrete velocities to neighbouring nodes:

$$f_i(\boldsymbol{x} + \boldsymbol{e}_i\Delta t, t + \Delta t) = \tilde{f}_i(\boldsymbol{x}, t) \tag{3.14}$$

External forcing is introduced in LBM by addition of fluid acceleration $\boldsymbol{a} = \boldsymbol{F}/m$ to the fluid velocity $\boldsymbol{u}$ in calculating the equilibrium distribution function via equation (3.13).

3.1.1 Colour gradient

All above equations describe single-phase flows. The Colour gradient is a method for LBM to simulate multi-phase flow of two immiscible fluids. The method could be generalised to more than two immiscible fluids, but we follow the implementation by Liu *et al.*[19], limiting ourselves to two.

Since there are two fluids, there are two separate distribution functions: f_i^R and f_i^B for red and blue fluid respectively. The total distribution function is the sum of both contributions: $f_i = f_i^R + f_i^B$ or $f_i = \sum_k f_i^k$ with k being one of the fluids.

Both fluids are treated separately, the streaming and collision step, equation (3.6) is performed for both fluids:

$$f_i^k(\boldsymbol{x} + \boldsymbol{e}_i\Delta t, t + \Delta t) - f_i^k(\boldsymbol{x}, t) = \Omega_i^k(f_i) \tag{3.15}$$

However, the collision operator in equations (3.6) and (3.15) differ, the latter being defined as:

$$\Omega_i^k = (\Omega_i^k)^{(3)} \left[(\Omega_i^k)^{(1)} + (\Omega_i^k)^{(2)}\right] \tag{3.16}$$

The total collision operator Ω_i^k and all three individual operators satisfy mass and momentum conservation as described in equations (3.8) en (3.9).

$(\Omega_i^k)^{(1)}$ is the collision operator from equation (3.4).

$(\Omega_i^k)^{(2)}$ is a two-phase operator generating a surface tension, defined as:

$$(\Omega_i^k)^{(2)} = \frac{A}{2}|\nabla\rho^N| \left(w_i \frac{(\boldsymbol{e}_i \cdot \nabla\rho^N)^2}{|\nabla\rho^N|^2} - B_i\right) \tag{3.17}$$

In this expression, w_i are the weights associated with the discretised velocities as discussed before and $B_0 = -1/3$, $B_{1-6} = 1/18$ and B_{7-18} in D3Q19. A is related to the surface tension by:

$$\sigma = \frac{4}{9}A\tau \tag{3.18}$$

with τ the relaxation time as used earlier in equation (3.4). Lastly, ρ^N is a normalised density, ranging from -1 to 1 and defined as:

$$\rho^N = \frac{\rho^R - \rho^B}{\rho^R + \rho^B} \tag{3.19}$$

Lastly, $(\Omega^k)^{(3)}$ is the recolouring operator, making the two fluids actually immiscible by segregating the fluids:

$$(\Omega_i^R)^{(3)}(f_i^R) = \frac{\rho^R}{\rho} f_i^* + \beta \frac{\rho^R\rho^B}{\rho^2} \cos(\phi_i) f_i^{eq}|_{\boldsymbol{u}=\boldsymbol{0}} \tag{3.20}$$

$$(\Omega_i^B)^{(3)}(f_i^B) = \frac{\rho^B}{\rho} f_i^* + \beta \frac{\rho^R\rho^B}{\rho^2} \cos(\phi_i) f_i^{eq}|_{\boldsymbol{u}=\boldsymbol{0}} \tag{3.21}$$

In the above two formulas $\rho = \rho^R + \rho^B$ trivially, f_i^* is the total distribution function after $(\Omega_i^k)^{(2)}$ has been applied, $f_i^{eq} = \sum_k f_i^{k,eq}$ and β is a parameter associated with the interface thickness. In this work $\beta = 0.7$ is for all simulations and ϕ_i is defined as:

$$\cos(\phi_i) = \frac{\boldsymbol{e}_i \cdot \nabla \rho^N}{|\boldsymbol{e}_i||\nabla \rho^N|} \tag{3.22}$$

3.1.2 Repulsion force

Section 3.1 briefly discussed how to put forces on the fluid in LBM and section 3.1.1 discussed how interfaces are created. This section treats a method for implementing a repulsion force between interfaces in LBM. More precisely, the objective is to implement a force that acts on an interface, pushing it away from a near interface. This repulsion force is the numerical implementation of a physical disjoining pressure. The implementation is similar to the work of Montessori at al.[21].

A fundamental problem with implementing a repulsion force, is that LBM is a simulation method that works locally. Lattice nodes only interact with the neighbouring nodes defined by the chosen DdQq model. This implies that there is no direct manner to tell whether two interfaces are near. The solution is using ρ^N as defined in section 3.1.1. Crossing an interface, ρ^N changes from -1 to $+1$ or vice versa. The further from an interface, the closer $|\rho^N|$ is to unity. This implies that exactly in the middle between two interfaces, the derivative of ρ^N is zero. On this location, the value of ρ^N is a measure for the distance these interfaces are apart.

Since we assume that the ρ^N follows the shape of a hyperbolic tangent, we also assume the value of ρ^N in the middle between interfaces is dependent on the distance to the interfaces in this same manner. After all, ρ^N can approximately be viewed as the combined contributions of both interfaces, both hyperbolic tangent. Figure 3.2 shows the dependency of ρ^N on the separation distance d. Indeed, a hyperbolic tangent perfectly fits, although a simple exponential function would work equally well since the hyperbolic tangent goes exponentially in the limit.

Note that there is no significant difference between different values of the surface tension σ. This is beneficial, since this makes it possible to vary the surface tension without affecting the working of the repulsion force. A more important issue is the absence of data points below $d = 6$. In such close proximity, the interfaces are not stable and from figure 3.2 it becomes clear why. If ρ^N approaches 0, it means interfaces start to merge. Use of the repulsion force should mainly be limited to situations where interfaces are separated enough, to avoid interference with the attractive forces of merging interfaces. The thickness of the interface is a key parameter here, and in the current work $\beta = 0.7$ is used. Be aware that the fitting parameters shown in figure 3.2 are only valid for $\beta = 0.7$.

Having proof that the value of ρ^N at the position where the derivative is zero can be used as measure for the strength of the repulsion force, we find these positions in the lattice by calculating the normal gradients of the ρ^N field:

$$\begin{aligned} \boldsymbol{n}(\boldsymbol{x}) &= \frac{\nabla \rho^N(\boldsymbol{x})}{|\nabla \rho^N(\boldsymbol{x})|} \\ \boldsymbol{n}_i'(\boldsymbol{x} + \boldsymbol{e}_i) &= \frac{\nabla \rho^N(\boldsymbol{x} + \boldsymbol{e}_i)}{|\nabla \rho^N(\boldsymbol{x} + \boldsymbol{e}_i)|} \end{aligned} \tag{3.23}$$

$\boldsymbol{n}$ is the normalised gradient of the ρ^N field and $\boldsymbol{n}_i'$ is the normalised gradient at neighbouring node located at $\boldsymbol{x} + \boldsymbol{e}_i$.

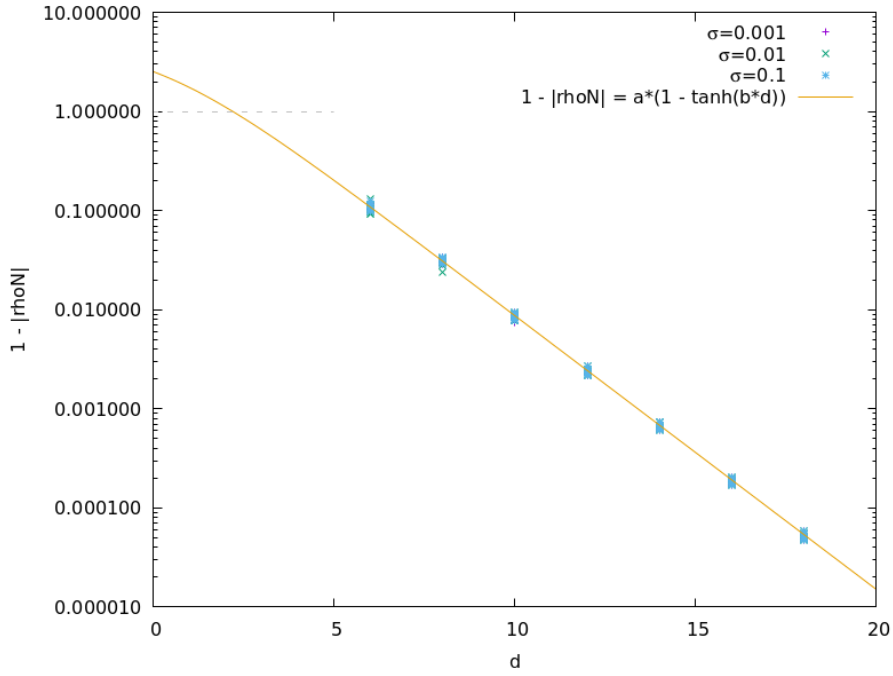

Figure 3.2: ρ^N in the middle between interfaces as function of separation distance. Fitting parameters: $a = 2.519$ and $b = 0.318$. The scatter of data points stems from the midpoint location relative to the lattice.

The repulsion force is calculated for each lattice node as:

$$\boldsymbol{F}_{rep} = \Pi\Psi\left(\rho^N\right)\sum_i H(-(\boldsymbol{n}\cdot\boldsymbol{e}_i)(\boldsymbol{n}_i'\cdot\boldsymbol{e}_i))H(\boldsymbol{n}\cdot\boldsymbol{n}_i'+\phi)\left(\frac{\boldsymbol{n}\cdot\boldsymbol{e}_i}{|\boldsymbol{e_i}|}\boldsymbol{n}+\frac{\boldsymbol{n}_i'\cdot\boldsymbol{e}_i}{|\boldsymbol{e_i}|}\boldsymbol{n}_i'\right) \tag{3.24}$$

Equation (3.24) is a somewhat complicated expression, which consists of a few distinct factors. The first Heaviside function H determines whether a neighbouring node pair located at $\boldsymbol{x}$ and $\boldsymbol{x}+\boldsymbol{e_i}$ spans over a minimum or maximum in the ρ^N field. In most cases, this Heaviside function yields zero since the gradients point in the same direction implying $(\boldsymbol{n}\cdot\boldsymbol{e}_i)(\boldsymbol{n}_i'\cdot\boldsymbol{e}_i) > 0$. The second Heaviside function is used for stability purposes by tuning the parameter ϕ. Note that ϕ must be between -1 and 1. For a lower the value of ϕ, fewer nodes have a repulsion force since the criterion for the dot product of the neighbouring gradients is stricter. This criterion is introduced to prevent repulsion between interfaces that make a large angle, or in the extreme case, repulsion between two parts of the same interface. A natural value is $\phi = 0$, implying a maximum angle between interfaces of 90° below which repulsion force is allowed.

Then, the part in equation (3.24) in large brackets determines the direction of the force, being the direction of the gradient, to ensure that the force is normal to the interface. Both $\boldsymbol{n}$ and $\boldsymbol{n}_i'$ are included, to prevent asymmetry between forces at node $\boldsymbol{x}$ and $\boldsymbol{x}+\boldsymbol{e}_i$. Unequal forcing would result in a net force, which could accelerate the fluid as a whole, which is obviously neither physical nor desirable.

Lastly, the two factors in front. Π is the repulsion force amplitude, determining its absolute strength. Ψ represents the relative strength of the repulsion force, which is dependent on the separation of the two interfaces and thus, as discussed, on ρ^N:

$$\Psi(\rho^N) = A\left(1-|\rho^N|\right)^{\chi(\delta)} \tag{3.25}$$

with the notion that A has approximately the same influence as Π, except for the fact that Ψ is cut off at a maximum value of 1. In the code used, $A = 2$ by default, which is an arbitrary value, and Π is used to vary the actual strength of the repulsion force. A last parameter is χ, dependent on the repulsion force range. We define the repulsion force range as the distance between the interface for which $\Psi = 0.5$ (recall that $0 \leq \Psi \leq 1$).

From figure 3.2 we learned that:

$$1-|\rho^N| = a(1-\tanh(bd)) \tag{3.26}$$

with a and b fitting parameters. Filling in equation (3.25) and equating $\Psi = 0.5$ for $d = \delta$:

$$\Psi = A(a(1-\tanh(b\delta)))^{\chi} = 0.5 \tag{3.27}$$

Solving for χ:

$$\chi(\delta) = \frac{\log(0.5/A)}{\log(a(1-\tanh(b\delta)))} \tag{3.28}$$

Filling in $A = 2$ and the found fitting parameters $a = 2.519$ and $b = 0.318$ fixes the value of χ for a given repulsion force range δ. Using equations (3.25) and (3.28), figure 3.3 shows Ψ as a function of d for various values of δ.

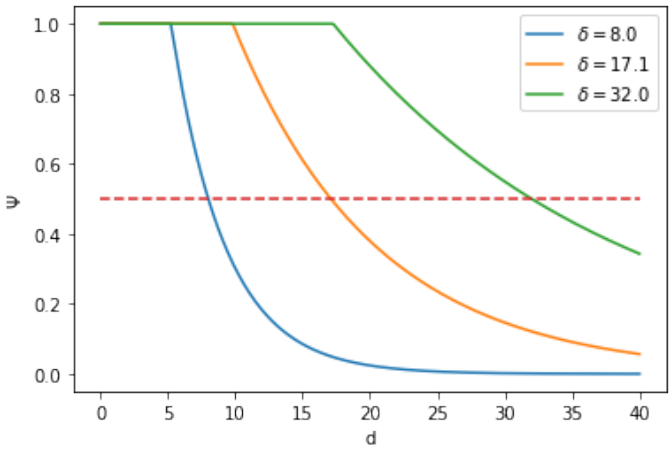

Figure 3.3: Relative repulsion force amplitude Ψ as function of separation distance of two interfaces.

A last remark on the used implementation of the repulsion force is that the force itself is not put on the interface but on fluid nodes in between. Two neighbouring nodes have exactly opposite forces which propagate naturally through the fluid towards the interface.

3.2 Critical binary droplet coalescence

To investigate the dependency of the droplet radius on turbulence intensity, we introduce the concept of critical droplet coalescence. Critical droplet coalescence is the threshold above which droplets coalesce; i.e. an impact with a slightly lower initial velocity of the droplets would cause the droplets to bounce off due to the repulsion force. The velocity needed for critical droplet coalescence is dependent on multiple parameters: the droplet radius, R, the surface tension, σ, the repulsion force amplitude, Π, the repulsion force range δ and if viscous dissipation is significant the viscosity, ν.

To study the critical droplet coalescence, LBM simulations are performed where two droplets, with certain characteristics, are launched towards each other. Since two droplet are involved in the collision, it is a binary droplet coalescence, a specific case of droplet coalescence in general. The droplets may or may not coalesce depending on the initial velocity of the droplets, using a fixed value for all other parameters. If the droplets do not coalesce, the initial velocity of the droplets is further increased in a subsequent simulation. If the droplets do coalesce the velocity is decreased. Using this midpoint finding algorithm, the initial velocity associated to the critical droplet coalescence is determined.

3.2.1 Initialisation

The purpose of performing a study on droplet collision via numerical simulations is to ultimately apply its conclusions to droplet coalescence in a (turbulent) emulsion. The droplet collision investigated here should be considered as a simplified model of an event occurring in an emulsion. In order to make this model as accurate as possible, some considerations should be taken into account.

First, if the goal is to study an oil-in-water emulsion, the density ratio should be around 1, which is simply achieved by setting $\rho_{blue} = \rho_{red} = 1$. Furthermore, we would like the viscosity to be of minor influence. After all, the purpose is to study turbulence in emulsions, implying high Reynolds number and thus low viscosity. The theoretical minimum in LBM simulations is $\tau = 0.5$, however for the simulation to remain stable $\tau = 0.55$ is the value which is used in the current study. Lastly, note that there is an important difference between giving the droplets an initial velocity artificially in a stagnant surrounding fluid (figure 3.4a) and including the surrounding fluid in the initialisation (figure 3.4c). The difference is major since the density ratio being 1 implies that also the surrounding fluid carries a significant percentage of the momentum. Including the surrounding fluid in the initialisation is the preferred method since this matches a situation found in emulsions better.

The two droplets are placed in a fluid domain with periodic boundary conditions such that their surfaces are 40 lattice nodes apart, without any initial velocity. From timestep zero, a body force acts on the full droplet volumes to give them a momentum towards each other. Note that the total momentum in the system remains zero due to the opposing forces of equal magnitude. When the droplets reach a separation of 30 lattice nodes between their closest interfaces, the body force is put to zero. At this point the droplets have a nonzero velocity in a surrounding fluid which is also moving (figure 3.4c). If compared to figure 3.4b the difference is major: due to the smooth forcing, no shock waves form, which is the case for initialising with nonzero velocity. What the exact effect of these shock waves is on the outcome of the droplet coalescence simulations has not been further investigated, however it can be expected that it definitely has influence.

However, also the situation in figure 3.4c cannot be considered as perfectly comparable to

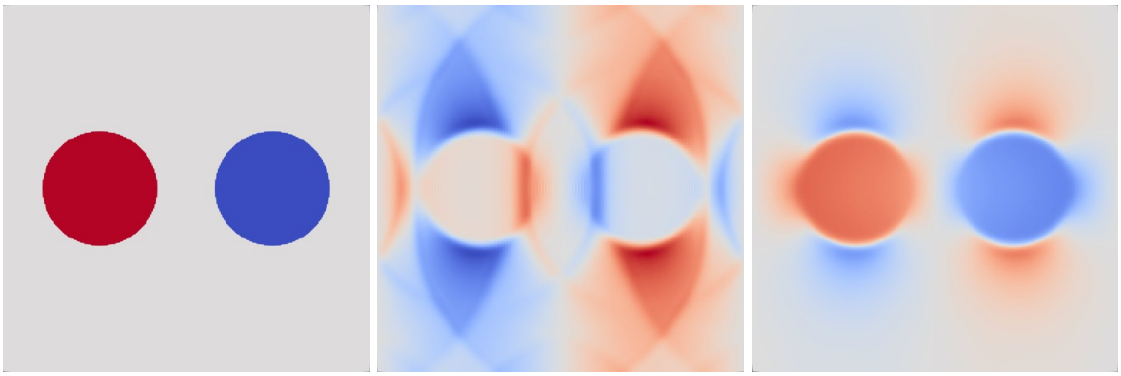

(a) (b) (c)

Figure 3.4: Velocity profile in the fluid domain. Red indicating x-velocity to the right and blue x-velocity to the left. (a) Droplets ($R = 40$) given initial velocity $v = 0.05$ at $t = 0$ in a stagnant fluid (b) Emerging shockwaves. Snapshot taken at $t = 200$ (c) Droplets (again $R = 40$) initialised from rest pushed together with a body force equal to 4.5×10^{-5} per lattice node in the droplet. Snapshot taken right after the force is set to zero, at timestep $t = 500$.

droplets in real emulsions. Note the opposing x-velocity below and above the droplets, coming from surrounding fluid moving from the front to the back of the droplet, taking the shortest route. This is a consequence of the periodic boundary conditions, which makes our setup different from a Stokes flow in an infinite domain, where surrounding fluid is flowing in the same direction as the fluid. The observed flow pattern is expected to have an impact on the amount of energy dissipation, which is naturally large for large velocity gradients.

For further analysis of the droplet coalescence simulations, the velocity that the droplets have at the moment that the body force is set to zero, is taken as the initial velocity of the droplet, v_0. This is a natural point to measure the initial velocity since this is the maximum velocity that the droplets will have; after this point the velocity will decrease due to the collision, under the effect of the disjoining pressure, energy dissipation and hydrodynamical interaction.

3.2.2 Energy balance in binary droplet coalescence

Section 2.3 provided theoretical formulas for calculating various energies in binary droplet coalescence. Here, we discuss how to extract this data from the numerical simulations.

Repulsion energy

The first major contribution to the energy balance that is investigated here, is the repulsion energy. This repulsion energy forms the energy barrier to overcome for successful droplet coalescence. As discussed in section 2.3, the repulsion energy is calculated by multiplying the repulsion force by the travelled distance. Recall equation (2.19), for two droplets the integral takes the form:

$$E_{rep} = \int_{A_{contact}} \int_{x_0(y,z)}^{x_1(y,z)} F_{rep}(x) dx dy dz \tag{3.29}$$

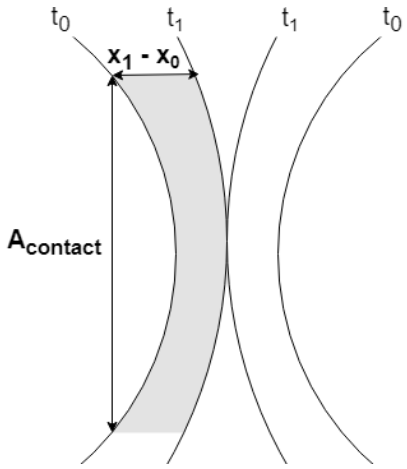

Figure 3.5: The grey area indicates the area over which the repulsion force between the droplets is integrated while the droplet surfaces displace from the initial location at t_0 to nearly-coalescence at t_1.

where y and z indicate the position on the contact surface of the droplet. Figure 3.5 provides a sketch of the area over which the repulsion force is integrated by equation (3.29).

In the code, the integral becomes a sum over the timesteps:

$$E_{rep} = \sum_{t=0}^{t_1} \sum_{j=0}^{N_y} \sum_{k=0}^{N_z} F^t_{N_x/2,j,k}(x^t_{j,k} - x^{t-1}_{j,k}) \tag{3.30}$$

where t_1 is the timestep of nearly-coalescence, or more specifically the timestep where the droplet velocity changes its sign. N_x, N_y and N_z are the domain size and x is the position of the interface. The repulsion force is only taken at the center of the domain ($N_x/2$) since the repulsion force is implemented on the nodes exactly in the middle of the two interfaces, which falls together with the center of the domain for this symmetric system.

As explained in section 3.1.2, the repulsion force acts on the nodes exactly in the middle between the interfaces. However, this does not necessarily mean that this is also the force that is experienced by the interface itself. To understand this, it must be noted that a force acting on any lattice node propagates through the fluid, towards an interface in this case. Due to viscosity, this propagated force diminishes. Especially in the current case, this effect is major since equal but opposite forces act on adjacent nodes. This effect can be seen as spurious velocities induced by the repulsion force. However, the effective repulsion force is needed to be filled in equation (3.30), needing to neglect the force lost in spurious velocity. This effective force is found by equating the repulsion force to a force of which we do know both the exact and effective magnitude. The relation between the imposed and experienced repulsion force is found by putting two droplets in the fluid domain, forcing them towards each other using a body force on the droplet volumes. This way, the repulsion force is balanced by the body force, which is constant: $F_{rep,effective} = F_{body,effective}$ (figure 3.6). This is a numerical simulation of the situation shown in figure 2.1a.

The body force acts on many lattice nodes and thus the force per node is relatively low, so

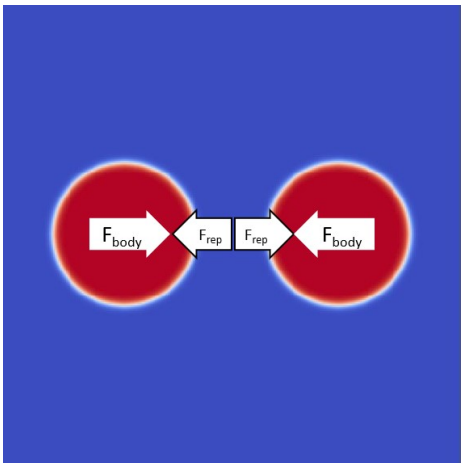

Figure 3.6: Force balance between the repulsion force and a body force on the droplet volume.

we assume that the force applied is equal to the force experienced: $F_{body,effective} = F_{body}$. And thus: $F_{rep,effective} = F_{body}$. We know the actual repulsion force applied, which allows calculating $\frac{F_{rep,effective}}{F_{rep}}$.

The repulsion force depends strongly on the separation distance between the droplets. Since the body force is constant, the droplet pair will oscillate like a spring-mass system, damping towards equilibrium. The oscillatory motion of the droplets and thus of the repulsion force, is seen from figure 3.7a. From this oscillation, the average is obtained which is taken as F_{rep}. Note that F_{rep} is much higher than the applied body force.

Five numerical simulations of balancing droplets have been performed, each for a different magnitude of the body force. Figure 3.7b shows the relation between F_{rep} and F_{body}. Recall that $F_{rep,effective} = F_{body}$, implying we can find the ratio $\frac{F_{rep,effective}}{F_{rep}}$ from the fit in figure 3.7b.

Surface energy

Obtaining the change in surface energy from the simulation is more straightforward than the repulsion energy. As mentioned in section 2.3, surface energy equals surface tension multiplied by surface area. In the numerical simulations, the surface tension σ is constant, measured in LBM units. The surface area can be obtained by integration over the interface in the ρ^N field. The change in surface energy is calculated by:

$$\Delta E_{surf}(t) = E_{surf}(t) - E_{surf}(0) \tag{3.31}$$

Energy dissipation

Ideally, energy dissipation plays no significant role in the droplet coalescence events studied. However, since the viscosity has a practical minimum in LBM simulations, this is not always the case, especially when the duration of the full coalescence event is large. Therefore it is relevant to measure the amount of energy dissipation in the simulations. It is not possible to extract this quantity

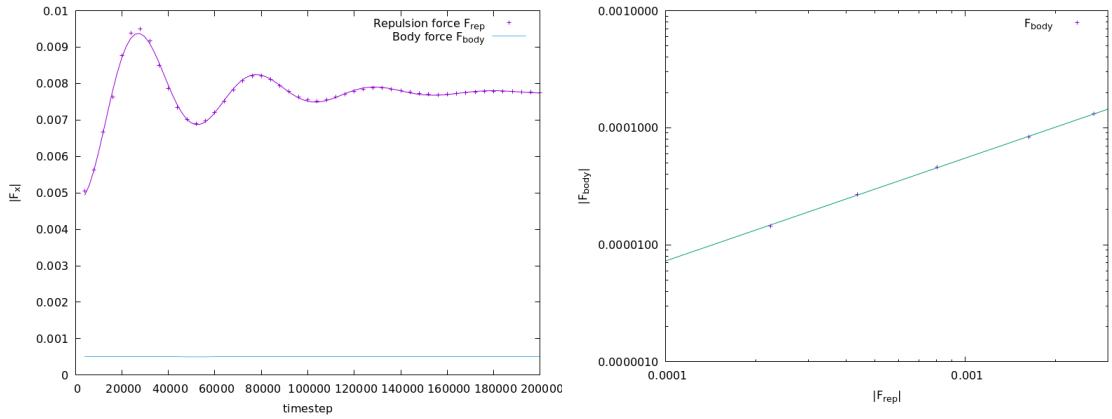

(a) (b)

Figure 3.7: (a) Repulsion force against time. The body force is kept at a constant value (b) Body force against repulsion force. From this plot we learn what value to use for equation (3.30), being the of $F_{rep,effective} = F_{body}$ given the value of F_{rep}.

directly, but it can be found by using the conservation of energy. As mentioned before, at some point, the body force on the droplets is set to zero. It is this point where the net velocity of the droplets is at its maximum. This point is considered as the beginning of the droplet coalescence process. On the other hand, the end of the droplet coalescence process is defined as the point where the net velocity of the droplet is zero again. Recall that nearly-coalescence is studied, so ideally the droplets come to perfect rest at this point.

Calculating the difference in total energy at these two points is the amount of energy that is dissipated (using equation (2.20)):

$$E_{diss}(t) = E_{kin}(0) + E_{rep}(0) + E_{surf}(0) - (E_{kin}(t) + E_{rep}(t) + E_{surf}(t)) \tag{3.32}$$

Generally, $E_{rep}(0)$ and $E_{kin}(t)$ both are nonzero. The former since the droplet has already travelled some distance and thus built up some repulsion energy, and the latter since due to internal and surrounding fluid motion the net droplet velocity may be zero whereas the total kinetic energy is not. However, this does not induce any problems since all quantities are easily obtained and thus the amount of energy dissipation can be calculated. More relevant, the relative energy dissipation can also be calculated, being $E_{diss}(t)/E_{kin}(0)$.

If the fraction of energy that dissipates during the droplet coalescence process is significant, there are two ways of accounting for this energy. The first option is most straightforward: including the term E_{diss} in the energy balance as by finding a theoretical expression which can be verified by the numerical results obtained.

A second option is to correct for energy dissipation. The energy dissipated is calculated as presented above. Furthermore, a factor f is found that indicates what fraction of the total energy is involved with net droplet movement at the moment the body force on the droplets is set to zero:

$$f = \frac{0.5\rho V v_0^2}{E_{tot}} = \frac{0.5\rho V v^2}{E_{kin}(0) + E_{rep}(0) + E_{surf}(0)} \tag{3.33}$$

Note the difference between $0.5\rho V v_0^2$ and $E_{kin}(0)$. These two quantities are fundamentally different: the former being the kinetic energy calculated only from the net movement of the droplet, the latter being the sum of the kinetic energy of all individual fluid nodes. f can vary between different simulation cases, but in general the value f is around 0.3.

Now, we state that the total energy dissipation is partly coming from the droplet movement and partly from other fluid motion in the domain. The (crude) assumption is made that the fraction that is coming from pure net droplet movement is equal to the fraction f calculated. Using this (rather crude) assumption, it becomes possible to predict the equivalent amount of initial kinetic energy required to observe the same critical coalescence event in case of zero energy dissipation (zero viscosity ν):

$$E_{kin,c}(0) \approx E_{kin}(0) - fE_{diss} \tag{3.34}$$

where the subscript c indicates that this is no real observed energy, but a corrected one. Having this quantity allows deriving other quantities from it, like the corrected Weber number, We_c, in contrast to the observed Weber number, We.

Chapter 4

Results

All formula presented in this section are two-dimensional and numerical results are all based on two-dimensional simulations. In section 4.1.5 the generalisation to three dimensions is made. The three-dimensional derivations can be found in the appendix.

4.1 Theoretical model

The objective is to provide a theory equivalent to Hinze, but for droplet coalescence. However, droplet coalescence is more complicated since (at least) two droplets are involved against only one in a droplet breakup process. The event of droplet coalescence is theoretically investigated by looking into the energy balance. The relevant energies involved are the kinetic energy, the surface energy and, optionally, the energy dissipation. By conservation of energy, we can write the energy balance for the system of two colliding droplets:

$$E_{kin} = c_1 E_{rep} + c_2 E_{surf} + c_3 E_{diss} \tag{4.1}$$

At the right hand side of the energy balance, the kinetic energy is not included since the droplet velocity and thus kinetic energy is zero on the moment of nearly-coalescence. In the following sections, E_{rep}, E_{surf} and E_{diss} are discussed separately.

4.1.1 Repulsion Energy

We consider the energy involved with the disjoining pressure and associated repulsion force. This force scales as $F_{rep} \sim \Pi A$ with A being the surface on which the force acts. To give a prediction for the contact area, the assumption is made that the magnitude of the disjoining pressure between two interfaces is equal to Π when the interfaces are within a distance δ, which is a simplification since we know from section 2.3 that the disjoining pressure decreases with distance smoothly. Figure 4.1 shows the nearly-coalescence of two spherical droplets. An expression for the contact area A is derived:

$$R^2 = (R - \delta)^2 + A^2$$

$$A = \sqrt{2R\delta - \delta^2}$$

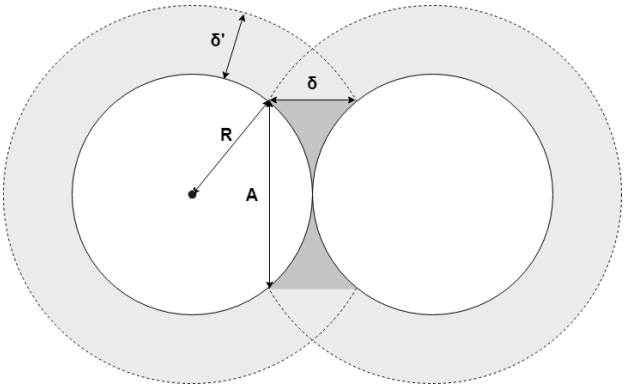

Figure 4.1: Critical coalescence of two circular droplets of radius R. The dark grey area indicates the region where the interfaces are within a range δ, defining the contact area, A. The light grey area indicates the region within a distance δ' from the droplet interface. For $\delta' \ll R$, $\delta \approx \delta'$. A is calculated from R and δ by geometry.

If we then assume $\delta \ll R$ and omit numerical prefactors:

$$A \sim \sqrt{R\delta} \tag{4.2}$$

Furthermore, note that this derivation only holds for spherical droplets. In case of droplet deformation, the contact area will increase. It is hard to give a mathematical prediction for this increase in contact area, so we use the following assumption:

$$\frac{R - R_0}{R_0} \sim We \tag{4.3}$$

This assumption is the same that will be used in section 4.1.2, where this result will be derived. If we assume that the contact area scales with droplet width, we can apply this to equation (4.2), yielding:

$$A \sim \sqrt{R\delta} + cR\,We \tag{4.4}$$

with c being a constant.

Now we know the repulsion force to be $F_{rep} \sim \Pi\sqrt{R\delta} + cR\,We$, the repulsion energy is simply derived by force times displacement, where the displacement is again δ since this is the distance over which the droplets travel:

$$\begin{aligned} E_{rep} &\sim \Pi\left(\sqrt{R\delta} + cR\,We\right)\delta \\ &= \Pi R\delta\left(\left(\frac{\delta}{R}\right)^{1/2} + c\,We\right) \\ &= \delta\sigma\left(\left(\frac{\delta}{R}\right)^{1/2} + c\,We\right)\tilde{\Pi} \end{aligned} \tag{4.5}$$

$\tilde{\Pi}$ is the dimensionless disjoining pressure, which we define as:

$$\tilde{\Pi} \equiv \frac{\Pi R}{\sigma} \tag{4.6}$$

4.1.2 Surface energy

The change in surface energy can be calculated by multiplying the surface tension σ by the change in surface area. This change in surface area is caused by the deformation from spherical droplets to non-spherical droplets during the coalescence process. Since there are three more energies involved in the process and we do not know their relative weight beforehand, it is hard to predict how much the deformation will be. For simplicity, the situation is compared to a droplet bouncing on a flat surface, as was experimentally studied by Laan *et al.*[18]. They proposed a general model for droplet collision on a surface consistent with a scaling of the droplet diameter $R/R_0 \sim We^{1/2}$ found in literature. This scaling is theoretically found from the energy balance where kinetic energy is converted to surface energy:

$$\begin{aligned} E_{kin} &\sim E_{surf} \\ \rho R_0^2 v^2 &\sim \sigma R \\ We &\sim R/R_0 \end{aligned} \tag{4.7}$$

Note that this result is in 2D, working out in 3D gives $\sim We^{1/2}$ as mentioned. An important remark is that obviously this model only works for $We > 1$, for a lower Weber number there is no substantial droplet deformation. However, in many of the simulations in the current work $We < 1$, which suggests investigating the scaling of $(R-R_0)/R_0$. This result would be obtained by replacing E_{surf} on the right-hand side of equation (4.7) by $\Delta E_{surf} \equiv E_{surf} - E_{surf,0}$.

Now, the surface energy is calculated as $E_{surf} = \sigma R$. For undeformed droplets, this gives $E_{surf,0} = \sigma R_0$, For deformed droplets it is slightly more complicated, however by using the proposed relation $(R - R_0)/R_0 \sim We$ we can work out:

$$\begin{aligned} \Delta E_{surf} &\equiv E_{surf} - E_{surf,0} \\ &\sim \sigma \left(R - R_0\right) \\ &\sim \sigma R_0 \, We \end{aligned} \tag{4.8}$$

4.1.3 Energy dissipation

The droplet collision process is hydrodynamically complicated. For an isolated droplet, Stokes flow is the analytical solution. In the binary droplet coalescence, the distance between the two interface decreases pushing the surrounding fluid to the sides. The area where this occurs naturally decreases, implying increasingly larger velocity gradients. All in all, it is hard to give a theoretical prediction for the energy dissipation due to these changing velocity gradients.

Another important note is that energy dissipation of a droplet moving through a fluid over a certain distance is dependent on the velocity of the droplet. Dimensional analysis yields the following result: energy dissipation rate scales with the velocity gradient squared and thus with

velocity squared: $\varepsilon \sim \nu \left(\frac{v}{L}\right)^2$ with ν the kinematic viscosity and L the characteristic length scale of the velocity gradient.

The time it takes for the droplet to travel a fixed distance d scales as $t \sim \frac{d}{v}$.

Combining the two gives that the total energy dissipated scales as: $E \sim \varepsilon t \sim \nu \left(\frac{v}{L}\right)^2 \frac{d}{v} \sim \nu d L^{-2} v^{-1}$.

The above equations state that droplets with lower velocity will have more energy dissipation during the process of coalescence, if we take an equal initial distance between the droplets. This dependency should be taken into account when interpreting numerical or experimental results.

4.1.4 Criterion for droplet coalescence

Having expressions for all involved energies, equation (4.1) can be filled in by using equations (4.5), (4.8) and for simplicity we assume $E_{diss} = 0$ for now:

$$\begin{aligned}
\rho R^2 v^2 &= c_1 \delta \sigma \left(\left(\frac{\delta}{R}\right)^{1/2} + c\ We \right) \tilde{\Pi} + c_2 \sigma R\ We \\
\rho R v^2 &= c_1 \frac{\delta}{R} \sigma \left(\left(\frac{\delta}{R}\right)^{1/2} + c\ We \right) \tilde{\Pi} + c_2 \sigma\ We \\
We &= c_1 \frac{\delta}{R} \left(\left(\frac{\delta}{R}\right)^{1/2} + c\ We \right) \tilde{\Pi} + c_2\ We
\end{aligned} \tag{4.9}$$

Rewriting towards a scaling of the dimensionless disjoining pressure gives:

$$c_1 \frac{\delta}{R} \tilde{\Pi} = (We - c_2\ We) \Big/ \left(\left(\frac{\delta}{R}\right)^{1/2} + c\ We \right) \tag{4.10}$$

Assuming small Weber number simplifies the above scaling to:

$$c_1 \left(\frac{\delta}{R}\right)^{3/2} \tilde{\Pi} = (1 - c_2)\ We \tag{4.11}$$

In this final equation, we still recognize all energies. On the right hand side: the kinetic energy and the surface energy whereas the term on the left hand side represents the repulsion energy barrier.

To conclude the theoretical investigation of energies involved in binary droplet coalesce, we give an overview of all expression to be verified in table 4.1

4.1.5 Length scale for droplets in turbulence

Recalling how the Hinze relation was derived from simple droplet breakup in section 2.1, here, the same procedure is followed, but now starting from droplet coalescence instead of droplet breakup. The starting point is equation (A.5), and if we assume the contribution of the surface energy to be of minor influence, the following simple relation remains:

Quantity	2D	3D
Contact area	$A \sim \sqrt{R\delta} + cR\ We$	$A \sim R\delta + cR^2\ We$
Repulsion energy	$E_{rep} \sim \delta\sigma \left(\left(\frac{\delta}{R}\right)^{1/2} + c\ We \right) \tilde{\Pi}$	$E_{rep} \sim R\delta\sigma \left(\frac{\delta}{R} + c\ We\right) \tilde{\Pi}$
Surface energy	$\Delta E_{surf} \sim \sigma R\ We$	$\Delta E_{surf} \sim \sigma R^2\ We$
Final scaling	$c_1 \left(\frac{\delta}{R}\right)^{3/2} \tilde{\Pi} = (1 - c_2)\ We$	$c_1 \left(\frac{\delta}{R}\right)^{2} \tilde{\Pi} = (1 - c_2)\ We$

Table 4.1: Overview of theoretical predictions for quantities relevant in critical binary droplet coalescence.

$$\begin{aligned} \left(\frac{\delta}{R}\right)^2 \tilde{\Pi} &\sim We \\ \delta^2 \tilde{\Pi} &\sim \rho v^2 R^2 \end{aligned} \tag{4.12}$$

Combining with equation (2.6) gives:

$$\begin{aligned} \delta^2 \Pi &\sim \rho \varepsilon^{2/3} R^{2/3} R^2 \\ R_{crit} &\sim \left(\frac{\delta^2 \Pi}{\rho}\right)^{3/8} \varepsilon^{-1/4} \end{aligned} \tag{4.13}$$

Note the introduction of the subscript in R_{crit} indicating it is the droplet radius or length scale associated with critical droplet coalescence. Furthermore note that the critical radius for droplet coalescence scales differently than for droplet breakup, the latter being the Hinze scaling $R_{crit} \sim (\frac{\sigma}{\rho})^{3/5} \varepsilon^{-2/5}$ (equation (2.10)). This implies that the two scalings cross and there exists a crossing point where the critical radii are equal. The position of this point can be expressed in terms of a dimensionless number:

$$\begin{aligned} R_{crit,breakup} &\sim R_{crit,coalescence} \\ \left(\frac{\sigma}{\rho}\right)^{3/5} \varepsilon^{-2/5} &\sim \left(\frac{\delta^2 \Pi}{\rho}\right)^{3/8} \varepsilon^{-1/4} \\ \frac{\rho^3 \Pi^5 \delta^{10}}{\sigma^8} \varepsilon^2 &\sim 1 \end{aligned} \tag{4.14}$$

It must be stressed that this result is preliminary. Where a critical radius has been verified for two-dimensional binary droplet coalescence, it has not yet been verified for droplets in emulsion. Realising that the two scalings $\varepsilon^{-2/5}$ and $\varepsilon^{-1/4}$ lie relatively close together, it is far from certain that this critical crossing point exists, e.g. in case the critical radius for coalescence scales differently in emulsions than in binary droplet coalescence.

	Π	δ	R	σ
1	1×10^{-6} - 2×10^{-4}	17.1	10	0.01
2	1×10^{-6} - 2×10^{-4}	17.1	20	0.01
3	2×10^{-6} - 5×10^{-4}	17.1	40	0.01
4	5×10^{-6} - 5×10^{-4}	17.1	80	0.01
5	5×10^{-7} - 1×10^{-4}	17.1	40	0.001
6	1×10^{-5} - 2×10^{-3}	17.1	40	0.1
7	1×10^{-5} - 5×10^{-4}	8	40	0.01
8	1×10^{-5} - 1×10^{-3}	32	40	0.01

Table 4.2: Overview of performed droplet coalescence simulations.

4.2 Numerical validation

Using Lattice Boltzmann numerical simulations the result presented in section 4.1 is verified. Specifically, equations (4.5), (4.8) and (4.11) are checked by performing simulations of binary droplet coalescence. Results presented in section 4.1.5 cannot be verified by these simulations, since a very specific and idealised setup is used. Only binary collisions with equally sized droplets and zero impact parameter are studied. Moreover, the surrounding fluid is stagnant at the beginning of all simulations, which is an idealised setup compared to actual turbulent emulsions.

4.2.1 Simulation cases

By performing simulations with varying parameters, the various proposed equations can be verified. The parameters that are varied are: the disjoining pressure amplitude, Π, the disjoining pressure range, δ, the droplet radius, R and the surface tension, σ. Of course many other parameters could be varied as well, e.g. the viscosity and the density ratio of fluid inside and outside the droplet. Additionally varying the impact parameter would undoubtedly reveal interesting physics. However, the four mentioned parameters are chosen because these are expected to be of relevance for the basic case of binary droplet coalescence as explained in section 2.3. Note that the initial droplet velocity is used to find the critical droplet coalescence for a given set of parameters. All parameters used are listed in table 4.2.

The different values of δ, R and σ in table 4.2 are chosen to find the dependency of critical droplet coalescence on these parameters. The specific value, $\delta = 17.1$ (instead of e.g. $\delta = 16$) is used since this appeared to be the default value in the used implementation of the repulsion force. Lastly note the wide range of values of Π, which consists of 6 to 8 separate simulations per line in the table, this gives a good data set to check the relation between Π and v. The boundaries of the ranges of Π are found by trial and error. The lower value is bounded by energy dissipation: low Π implies low v and if these values are too extreme, the droplet will come to rest before coalescing. The upper bound of Π is determined by the stiffness of the droplet: too high Π and thus high v causes the droplet to break apart instead of coalescing (figure 4.2).

These violent cases are not included in the analysis of critical binary droplet coalescence. Although three-dimensional simulations are not included in this work, it seems that in three dimensions this is not an issue since radially symmetric droplet do not break up in two parts. Instead a hole can form in the middle, resulting in a donut shaped droplet which can still be considered a single

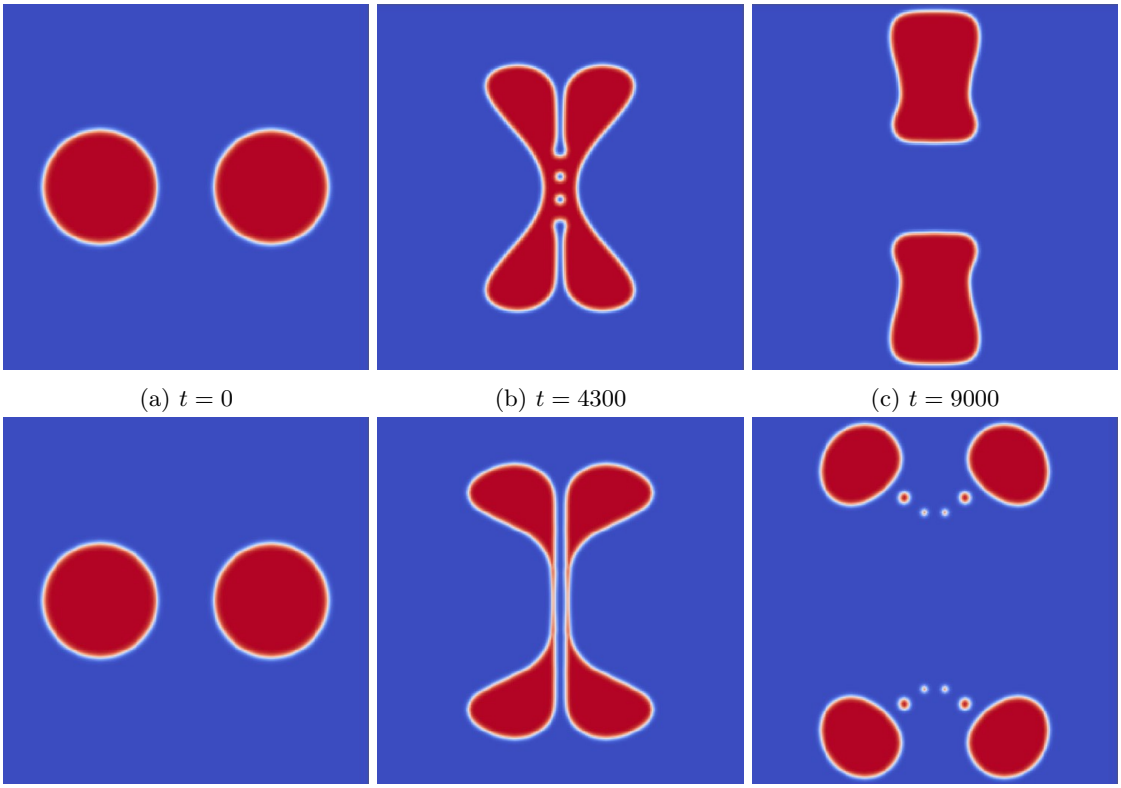

(a) $t = 0$ (b) $t = 4300$ (c) $t = 9000$

(d) $t = 0$ (e) $t = 4500$ (f) $t = 10000$

Figure 4.2: Droplet breakup by high disjoining pressure and high initial velocity. A distinction can be made between breakup before and after coalescence. (a)-(c) Droplet breakup before coalescence. Parameters: $R = 40$, $\sigma = 0.01$, $\Pi = 1 \times 10^{-3}$, $\delta = 5.0$ and $v = 2.4 \times 10^{-2}$ (d)-(f) Droplet breakup after coalescence. Parameters: $R = 40$, $\sigma = 0.01$, $\Pi = 2 \times 10^{-3}$, $\delta = 5.0$ and $v = 2.8 \times 10^{-2}$.

droplet.

In between those lower and upper boundaries are simulation cases over a couple orders of magnitude. Figure 4.3 illustrate the outcome of some of these nearly-droplet coalescence simulations.

Note the spherical shape of the droplets for $\Pi = 2 \times 10^{-6}$, the slight deformation for $\Pi = 5 \times 10^{-5}$ and the substantial deformation for $\Pi = 5 \times 10^{-4}$. The explanation is the correlated velocity, which is higher for higher Π. Higher droplet velocity also implies a substantial shorter simulation time as can be seen in figure 4.3. This shorter simulation time is indirectly the explanation for the droplets being closer to each other for higher Π: since the simulations take a shorter time, more iterations were performed finding critical coalescence. In general, the closer to critical coalescence, the closer the two droplets are.

As discussed in section 3.2.2, the repulsion energy, surface energy and energy dissipation could be obtained. All are plotted against time in figure 4.4. Note how all energies begin at zero since the droplets start at rest. The period that the droplets are forced with a body force is clearly visible by the kinetic energy going up linearly, after which it reaches a maximum. After this maximum, the total energy immediately starts to decrease due to energy dissipation.

A few things should be mentioned about figure 4.4. First, the total energy is not simply the sum of the kinetic energy, repulsion energy and surface energy. This is because the kinetic energy plotted is calculated as $0.5\rho V v^2$ with v the net velocity of the droplet. The kinetic energy used to calculated the total energy is the sum of the kinetic energy of all individual fluid nodes.

Furthermore, the surface energy in figure 4.4a oscillates substantially. However, this is also the case in the other two plot but is more visible due to the scale on the y-axis. Recall that the droplet velocity is lower in case of lower Π, which translates into lower kinetic and total energy in the system. The oscillation is not considered problematic, although it clearly affects the accuracy of the energy calculations. The oscillation itself is believed to originate from droplet oscillation inducing an inaccuracy in the measurement of surface area on timescales longer than the oscillation period. LBM simulations of droplet oscillation have been performed by among others Guskova *et al.*[12], but was not further investigated in this work.

Also the measurement of the repulsion energy cannot be considered fully accurate, which can be seen in figure 4.4b. After the nearly-coalescence event, the total energy increases a little, which should not be possible. The explanation is an error originating from the calculation of the repulsion energy, as discussed in section 3.2.2.

Where figure 4.3 shows nearly-coalescence of droplets, figure 4.5 shows the case where initial velocity is slightly higher and thus the droplets do coalesce.

The shape of the droplet at the latest timestep is dependent on how early the simulation is stopped. Trivially, the coalesced droplet will relax to a spherical shape after performing a damped oscillation. Furthermore, compare the timestep of the middle figures in 4.3 and 4.5. Ideally, these timesteps are close together because in the limit of critical droplet coalescence the two cases approach each other.

The equations found in section 4.1 are verified by plotting the energies against Weber number and will be discussed separately in the following sections.

4.2.2 Repulsion energy

Equation (4.5) is verified by plotting the energy stored in the repulsion between the droplets at the moment of nearly-coalescence against the Weber number (figure 4.6a). Rescaling by $\frac{R^{1/2}}{\sigma\delta^{3/2}}$

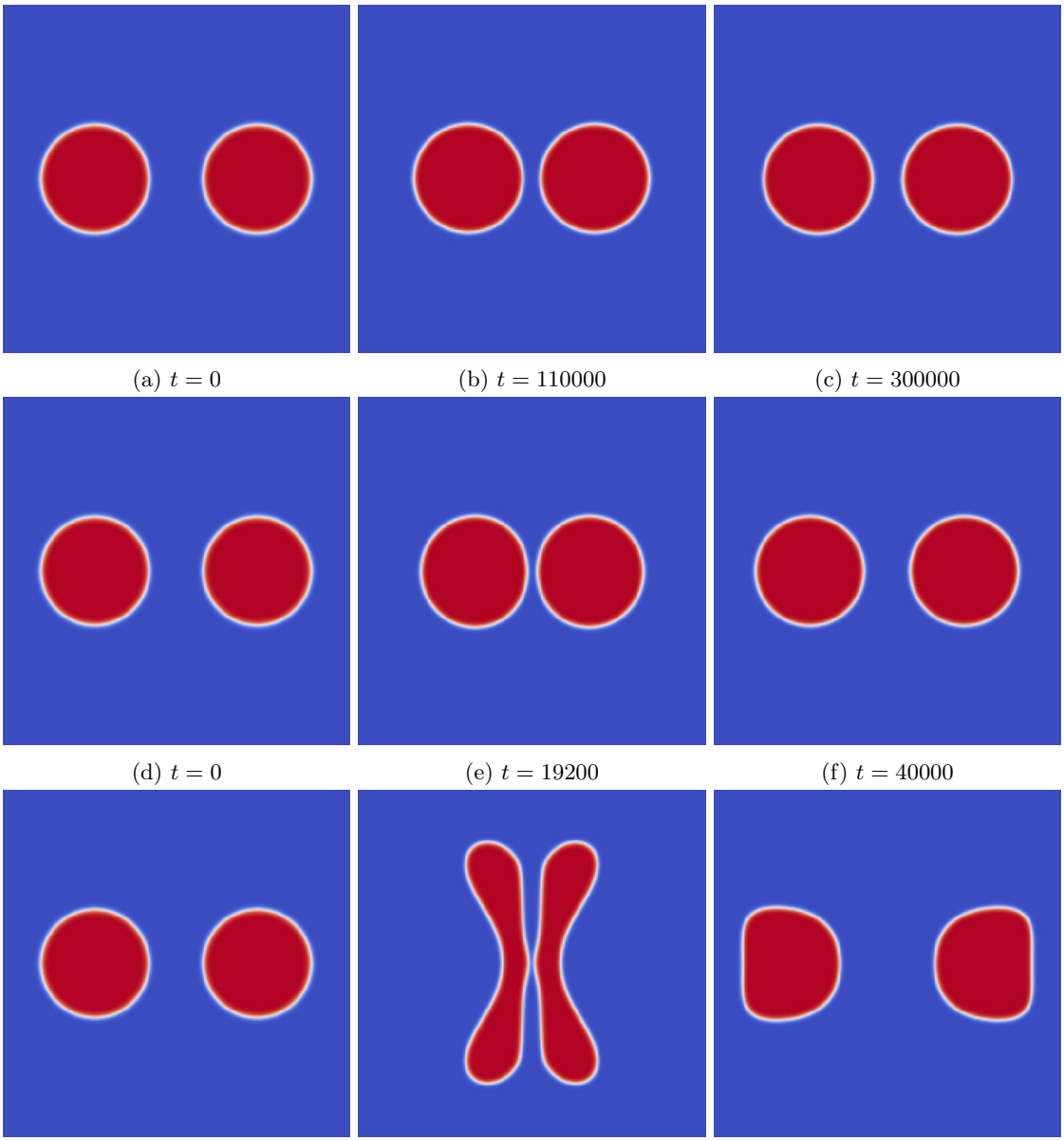

(a) $t = 0$ (b) $t = 110000$ (c) $t = 300000$

(d) $t = 0$ (e) $t = 19200$ (f) $t = 40000$

(g) $t = 0$ (h) $t = 5000$ (i) $t = 15000$

Figure 4.3: Nearly droplet coalescence of two droplets with parameters $R = 40$, $\sigma = 0.01$, $\delta = 17.1$ and $\Pi =$ (a)-(c) 2×10^{-6} (d)-(f) 5×10^{-5} (g)-(i) 5×10^{-4}.

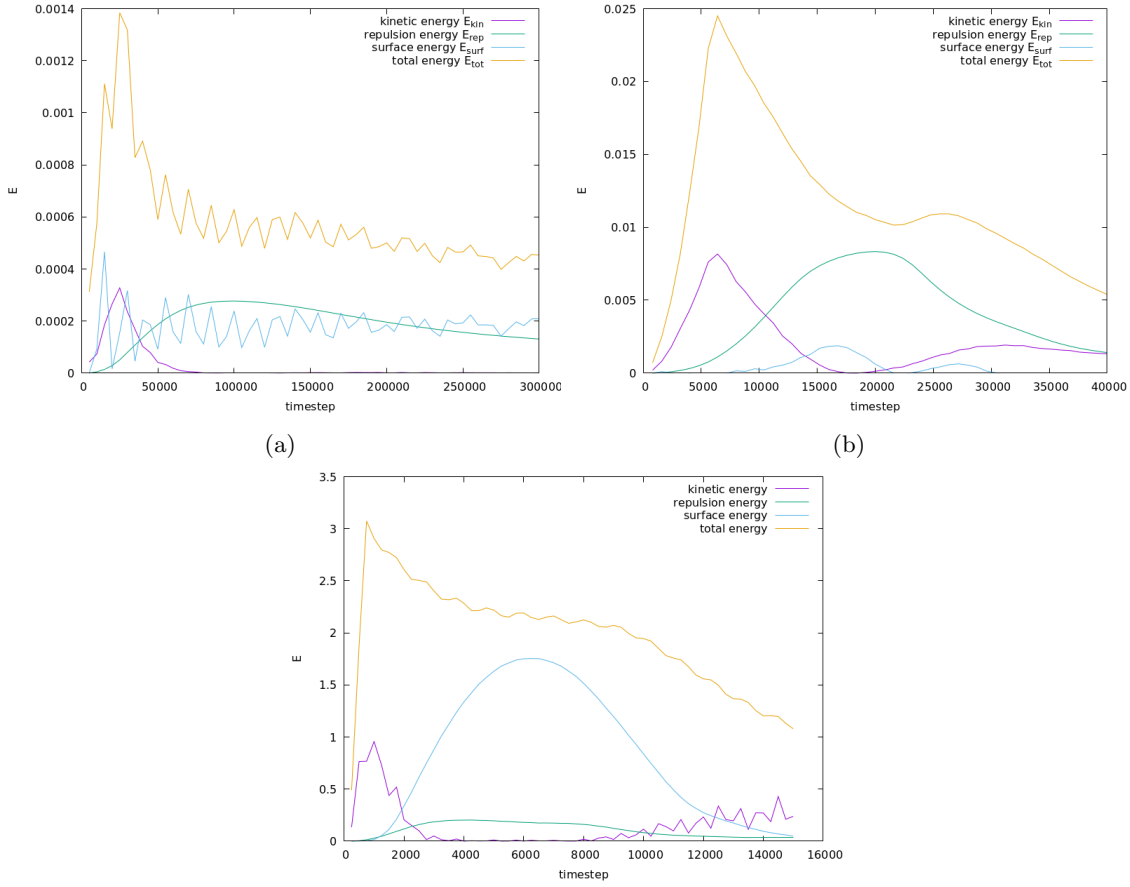

Figure 4.4: Evolution of energies involved in droplet coalescence, with $E_{kin} = 0.5\rho V v_{droplet}^2$, E_{rep} calculated as discussed in section 3.1.2, $E_{surf} = \sigma A_{surf}$ and $E_{tot} = \sum_{i=0}^{lattice} 0.5\rho v_i^2 + E_{rep} + E_{surf}$. Parameters: $R = 40$, $\sigma = 0.01$, $\delta = 17.1$ and $\Pi =$ (a) 2×10^{-6} (b) 5×10^{-5} (c) 5×10^{-4}.

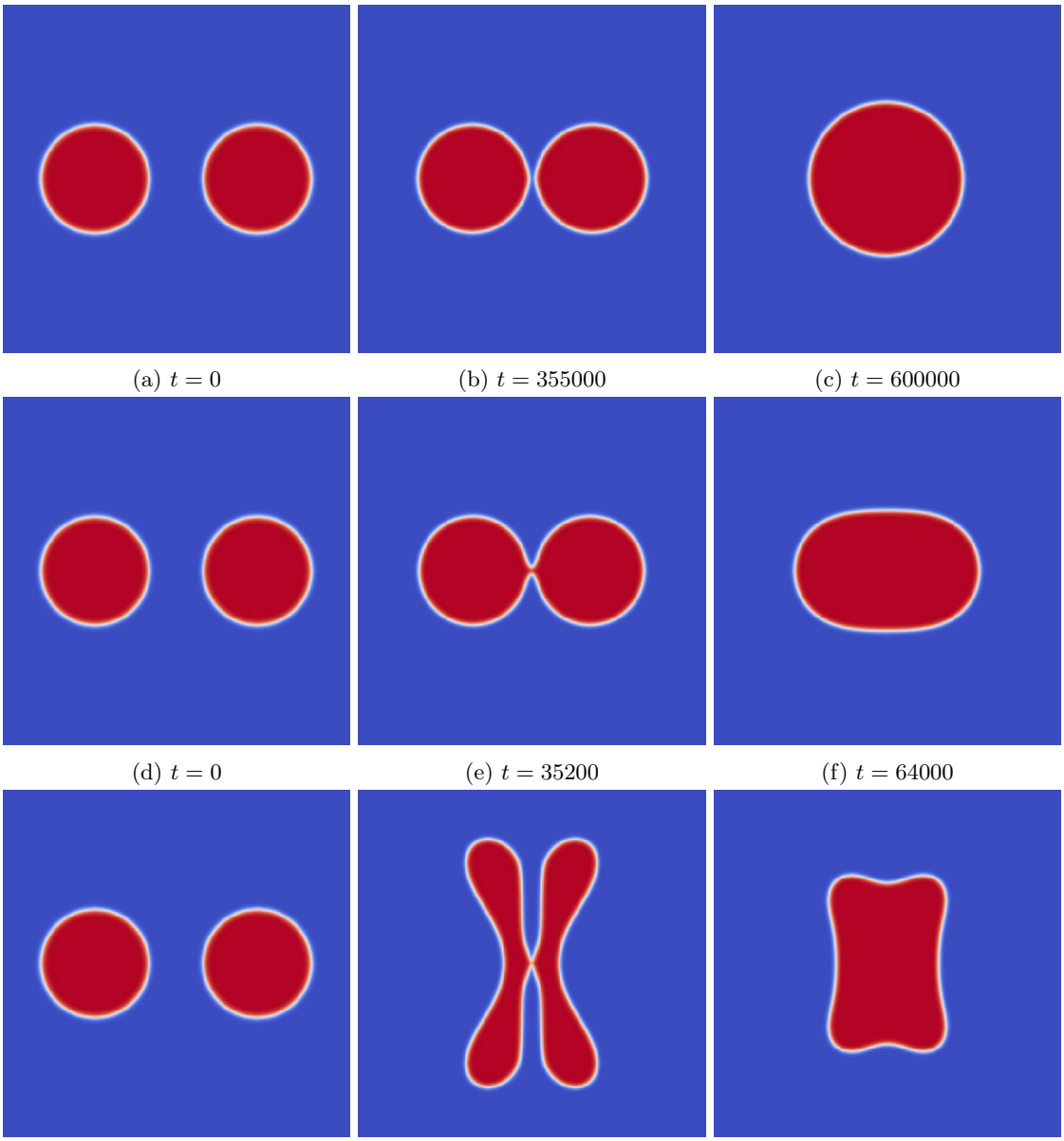

(a) $t = 0$ (b) $t = 355000$ (c) $t = 600000$

(d) $t = 0$ (e) $t = 35200$ (f) $t = 64000$

(g) $t = 0$ (h) $t = 5250$ (i) $t = 15000$

Figure 4.5: Droplet coalescence of two droplets with parameters $R = 40$, $\sigma = 0.01$, $\delta = 17.1$ and $\Pi =$ (a)-(c) 2×10^{-6} (d)-(f) 5×10^{-5} (g)-(i) 5×10^{-4}.

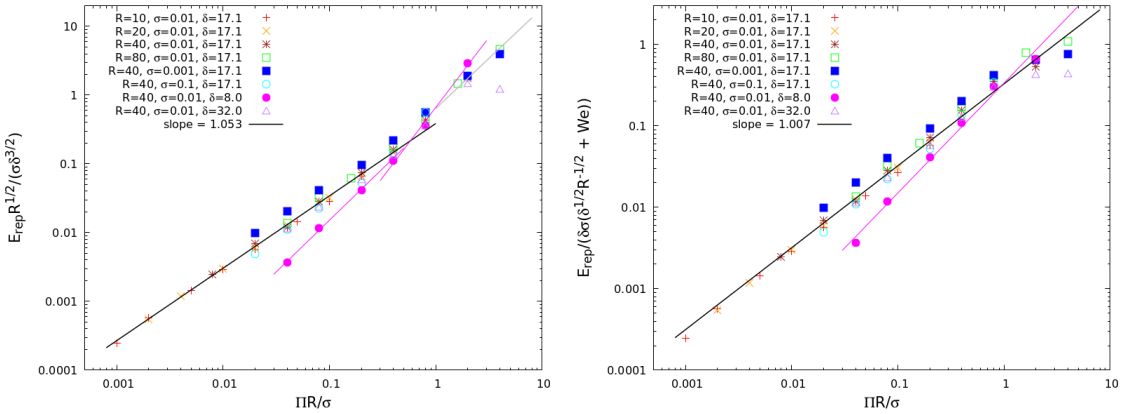

(a) (b)

Figure 4.6: (a) Repulsion energy as function of the dimensionless disjoining pressure. Two regimes are recognizable in the curves. The case corresponding to $\delta = 8.0$ is not included in the fit since it is considered an outlier. (b) Rescaled repulsion energy as function of dimensionless disjoining pressure. By including droplet deformation as function of the Weber number, the data seems to scale as $\sim \tilde{\Pi}$ slightly better, but the quality of the fit is not significantly better.

according to equation (4.5) shows the expected unit slope. Rescaling with a more complex factor $\delta\sigma\left(\left(\frac{\delta}{R}\right)^{1/2} + We\right)$ (figure 4.6b) only improves the fit quality slightly. It is an indication that the additional contact area caused additional repulsion energy and scales as $\sim We$, but yet far from convincing.

Figures 4.6a and 4.6b show that the case $\delta = 8.0$ is an outlier. The explanation is found in the implementation of the repulsion force in LBM as discussed in section 3.1.2. For shorter ranges δ the specified value of δ becomes less accurate since the range interferes with the interface thickness. Also simulations with $\delta = 4.0$ have been performed, however were not included in this work since those appeared to be highly unstable and inaccurate. Apparently, $\delta = 8.0$ is around the lower boundary for the repulsion force range. Data points with $\delta = 32.0$ do match the other data.

4.2.3 Surface energy

In section 4.1.2 the theory was discussed that the droplet diameter scales with Weber number and from this relation it was worked out that the change in surface energy also scales with the Weber number.

Figure 4.7 shows how the maximum droplet radius changes with increasing the Weber number. For most cases, the scaling is around $(R - R_0)/R \sim We$ as expected. Closer inspection of the graph shows that the widest scatter is for low Weber number and thus small deformations, which is logical since then inaccuracies in the measurement have the largest impact. Furthermore, looking at the individual data sets show that they roughly follow a unit slope for large Weber number and scatter more at low Weber number. Lastly note that, in contrast to results later presented, no correction for energy dissipation is included here. This does not have large implications for droplet

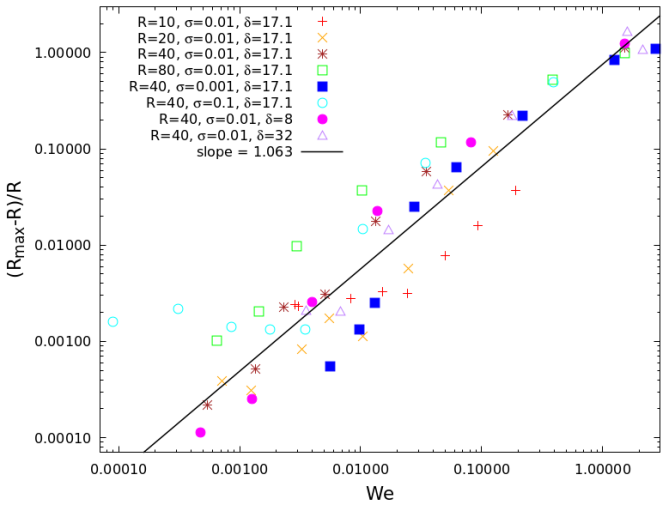

Figure 4.7: Relative change in droplet radius as function of the Weber number. The scaling is as predicted by theory, although the scatter is significant.

deformation since deformation happens early in the coalescence process, before much energy has dissipated. However, for smaller droplets, energy dissipation has a larger effect, which is visible in figure 4.7 by smaller relative deformation for smaller radius at equal Weber number.

Figure 4.8 shows the dependency of surface energy on Weber number.

Measurement of the surface energy encounters the same problem as measuring the deformation: at small deformation the measurement becomes inaccurate. From figure 4.8 we roughly estimate that $E_{surf}/(R\sigma)$ can be determined down to 5×10^{-4}. This observation is based on individual data sets branching off towards this value, decreasing the Weber number.

Having noted these outliers and excluded those from the fit, a scaling around $\sim We^{4/3}$ for the surface energy is found, whereas the maximum droplet radius showed a scaling $\sim We$. The explanation this scaling differs from the expected theory is that we assumed the droplets to have a certain shape upon deforming, which appears not to be accurate (figures 4.9a and 4.9b).

The discrepancy between figures 4.9a and 4.9b is clear: the actual surface area is much larger than accounted for. No reasonable new theory could be found to account for this extra surface area, so from now on, as opposed to equation (4.8), we will use the empirical relation:

$$\Delta E_{surf} \sim \sigma R\, We^{4/3} \tag{4.15}$$

Energy Dissipation

As stated earlier, energy dissipation can be significant in the performed simulations. Figure 4.10a shows that energy dissipation can be over 90%, which is especially the case for small droplets.

Figure 4.10b is obtained from figure 4.10a by rescaling the y-axis by $(R/d)^{1/2}$ with $d = 15$ the distance over which a droplet travels from the moment of maximum velocity to nearly-coalescence. This rescaling is empirical, where minimising the scatter was leading neglecting the outliers for the

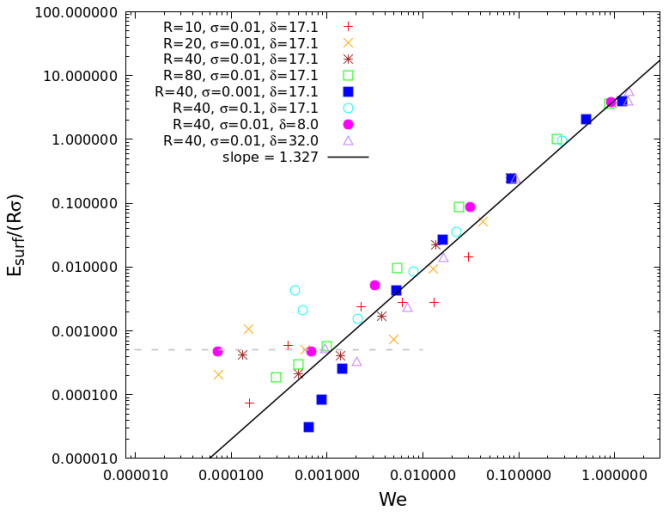

Figure 4.8: Surface energy as function of the Weber number. The surface energy on the y-axis has been rescaled to make it dimensionless. The dashed line shows a rough estimate of lowest value for which accurate results can be obtained. Data points floating around this value have not been taken into account for the fitted line.

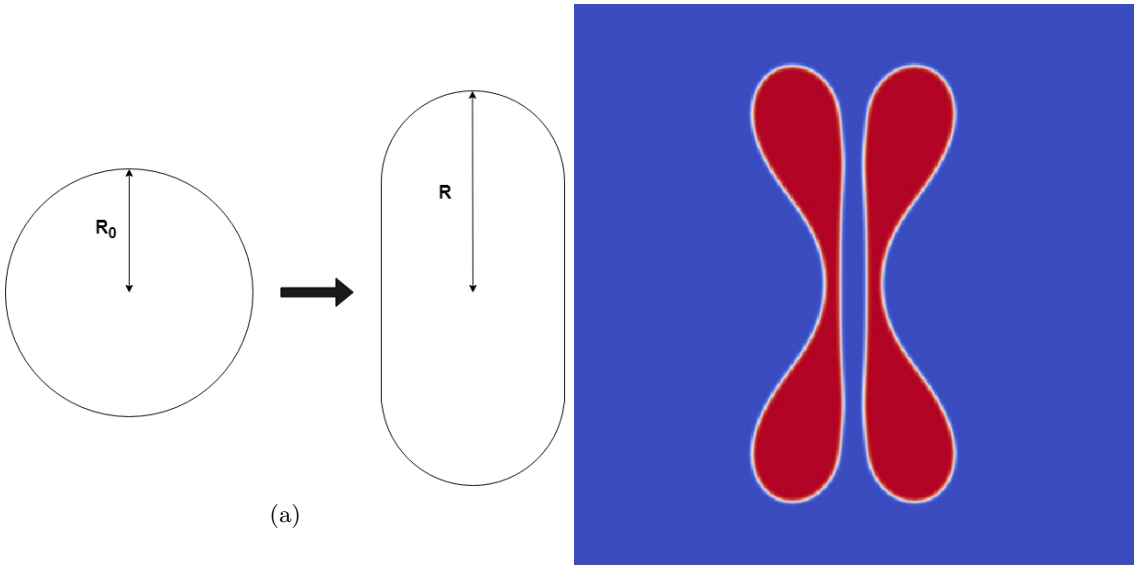

(a)

(b)

Figure 4.9: (a) Assumed droplet shape in section 4.1.2 (b) Observed droplet shape at maximum droplet diameter. Parameters: $\Pi = 5 \times 10^{-4}$, $\delta = 17.1$, $R = 80$ and $\sigma = 0.01$

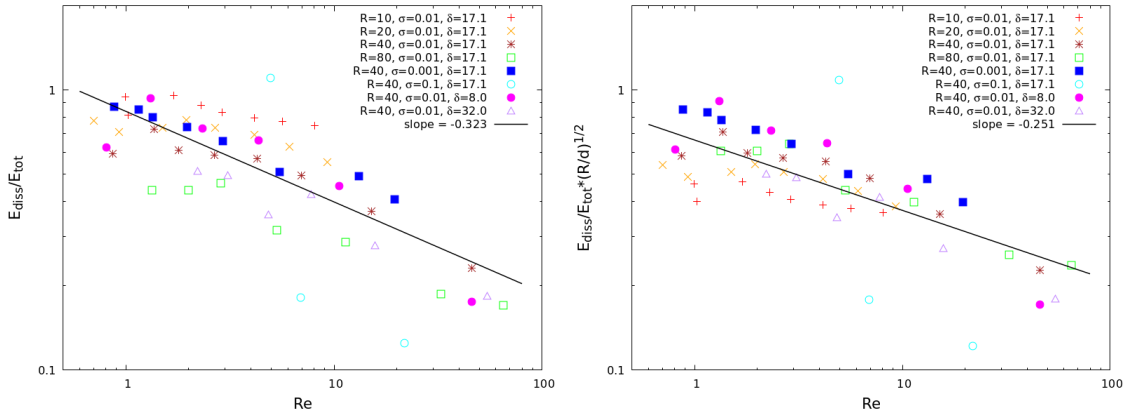

(a) (b)

Figure 4.10: (a) Relative energy dissipation as function of Reynolds number (b) Empirical rescaling of relative energy dissipation as function of Reynolds number

case $\sigma = 0.1$. Especially, the overlap between data for different radii was pursued. Although the scatter is slightly less, the presented formula is far from convincing based on the presented data.

However, using the empirical rescaling found, the energy dissipation for the process of droplet coalescence would scale as:

$$E_{diss} \sim E_{kin} \left(\frac{d}{R}\right)^{1/2} \tag{4.16}$$

The above equation can be used to fill in the energy balance equation (4.1). Note that the travelled distance d is used here to make the scaling dimensionally correct. However, in all simulations this distance was kept constant, so the scaling with d has not been verified.

4.2.4 Criterion for droplet coalescence

Using the scaling with Weber number found in section 4.2.3 (equation (4.15)), equation (4.11) is altered to:

$$c_1 \left(\frac{\delta}{R}\right)^{3/2} \tilde{\Pi} = We - c_2 \, We^{4/3} \tag{4.17}$$

Recall that energy dissipation was omitted to obtain this result in section 4.1, but cannot be neglected according to the results in section 4.2.3. To account for this discrepancy, the Weber number We is simply replaced by We_c which is the Weber number corrected for energy dissipation as discussed in section 3.2.2:

$$c_1 \left(\frac{\delta}{R}\right)^{3/2} \tilde{\Pi} = We_c - c_2 \, We_c^{4/3} \tag{4.18}$$

The dimensionless disjoining pressure is plotted against Weber number (figure 4.11a). Two distinct branches are visible, which is in accordance with Yoon *et al.*[29]. The left branch corresponds

to low Weber number and low dimensionless disjoining pressure resulting in spherical droplet during the entire droplet coalescence process (recall figure 4.3b). On the other hand, the right branch corresponds to the region where droplets deform and thus the change in surface energy becomes significant as can be seen from the bend in the plots. This can be rephrased to an interpretation of the dimensionless disjoining pressure: $\tilde{\Pi}$ tells whether droplets are susceptible to deformation. Realising that $\tilde{\Pi}$ is defined as disjoining pressure over Laplace pressure intuitively confirms this explanation.

We do not see overlap for low Weber number, as expected. However, there is some overlap for higher Weber number, the region where the surface energy becomes important. Note this overlap was not expected based on equation (4.17)

Plotting the dimensionless disjoining pressure against corrected Weber number (figure 4.11c), in order to check equation (4.18) exhibits the same behaviour. If we rescale the y-axis by $\left(\frac{\delta}{R}\right)^{3/2}$, we see significant overlap in the left branch, confirming the left part of equation (4.18). Omitting all data point where σ or δ is varied is even more convincing (figure 4.12), although only confirming the relation with R. On the other hand, the overlap in the right branch has disappeared, together with the overlap without rescaling, suggesting that c_2 is not constant.

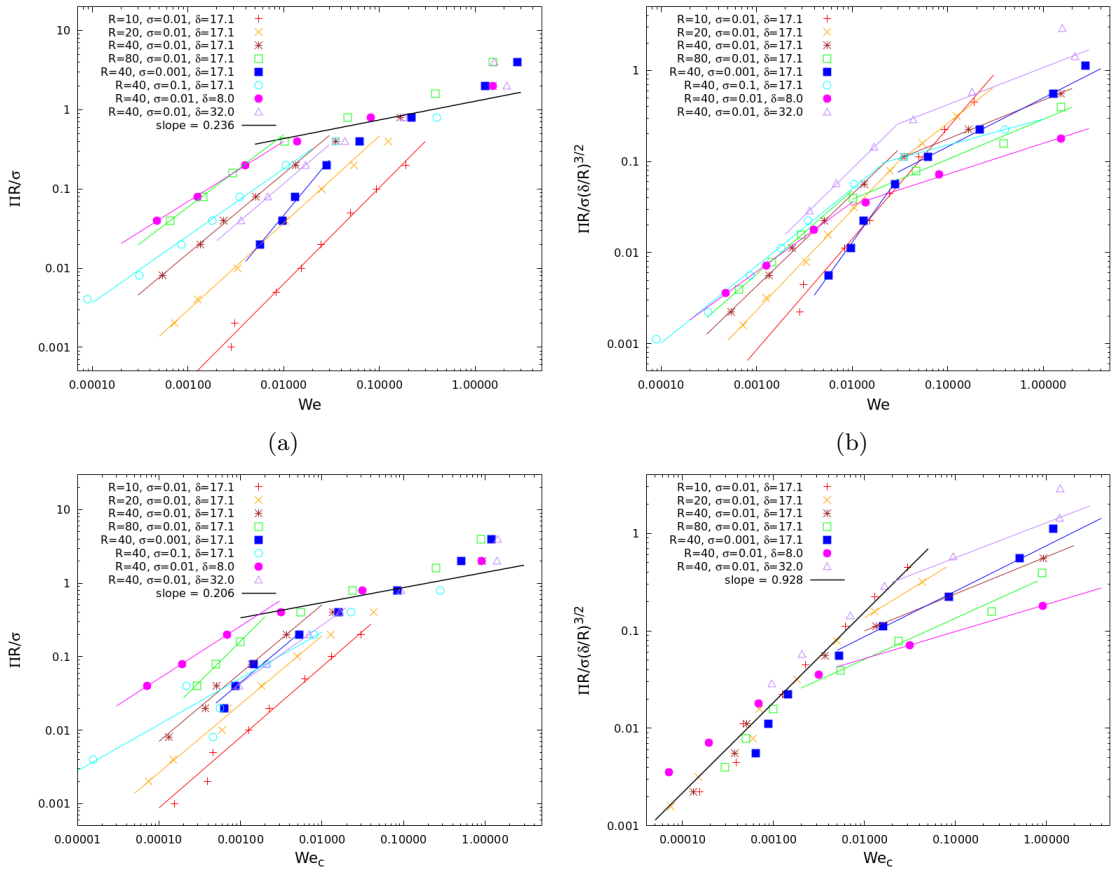

Figure 4.11: Dimensionless disjoining pressure against Weber number (a) Uncorrected (b) Uncorrected and rescaled (c) Weber number corrected for energy dissipation (d) Weber number corrected for energy dissipation and rescaled.

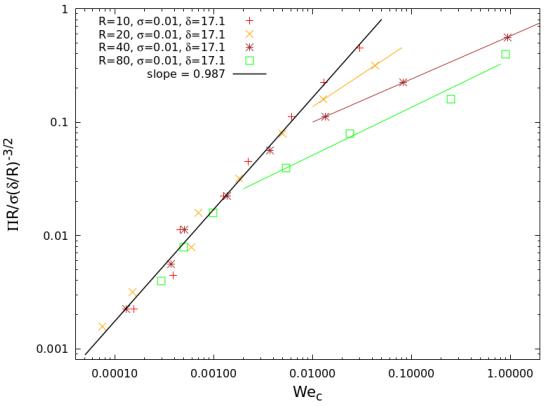

Figure 4.12: Dimensionless disjoining pressure against Weber number for a limited data set where only the droplet radius is varied.

Chapter 5

Conclusion

We suggested a second length scale in turbulent emulsions, in addition to the classical Hinze length scale. This second length scale is the critical radius for droplet coalescence, above which droplet can coalesce and below which they cannot due to a disjoining pressure.

The theory presented has not yet been verified by numerical simulations or experiments. Using Lattice Boltzmann simulations a first step in this process has been taken, by verifying a criterion for critical droplet coalescence in two-dimensional binary droplet collisions. Especially the region where droplets remain more or less spherical and thus changes in surface energy are insignificant shows a good agreement between theory and simulation. The relation in this region is $\left(\frac{\delta}{R}\right)^{3/2}\tilde{\Pi} \sim We$, in two dimensions. Here, $\tilde{\Pi} = \frac{\Pi R}{\sigma}$ is a newly introduced dimensionless number in fluid mechanics defined as the ratio between the disjoining pressure and the Laplace pressure. The dimensionless disjoining pressure relates to the deformability of droplets due to disjoining pressure.

The next step in verifying the theory for critical droplet coalescence is generalisation to three dimensions, which is expected to be relatively easy. After that, statistics of droplet coalescence in emulsions should be obtained from numerical simulations in order to investigate whether the criterion also holds in the far more complex environment of turbulent emulsions.

Chapter 6

Discussion and outlook

Although the performed numerical simulations support the presented theory, there are definitely limitations one should be aware of. First, note that only a specific case is verified: two identically sized droplets, colliding at zero impact parameter. Moreover, the simulations are all two-dimensional. Generalising the model to nonzero impact parameter does not have priority in further research. However, some three-dimensional simulations have been performed, though not included in the current work. Verifying the three-dimensional model is the first step on the road map validating the model for critical droplet coalescence.

Secondly, also the numerical simulations presented in this work have some important limitations to take into account when interpreting results and when setting up simulations for following work.

6.1 Further validation of proposed length scale

As mentioned before, the results in section 4.1.5 have not yet been verified. It is beyond the scope of this work to perform simulations of turbulent emulsions. These simulations would require much more computational resources since the fluid domain must be large to ensure droplets large enough. Performing these larger simulations is considered as a next step validating the proposed theory since it gives the opportunity to study droplet coalescence in turbulent emulsions, instead of in an isolated environment. Special attention should be paid to the question whether the proposed scaling holds for different ratios of droplet size and for nonzero impact parameter.

Note that breakup and the associated Hinze scaling will also play a role in these simulations. Since the two length scales in equations (2.10) and (4.13) scale differently with turbulent intensity, this gives rise to interesting physics with a critical turbulent intensity ε_{crit} calculated by equation (4.14). The sketch in figure 6.1 shows the scaling of the two length scales and the critical turbulent intensity.

Consider an emulsion with large oil droplets in water. Upon increasing the turbulent intensity (i.e. faster stirring), the maximum droplet radius will decrease along the Hinze scaling. If the amount turbulence is decreased again, the droplet size will increase accordingly (moving back and forth along the red line in figure 6.1). However, if the turbulent intensity surpasses the value of ε_{crit}, the droplets have become too small to coalesce and should remain small upon decreasing the turbulence. This phenomenon is called hysteresis and is indicated as the region below the blue line

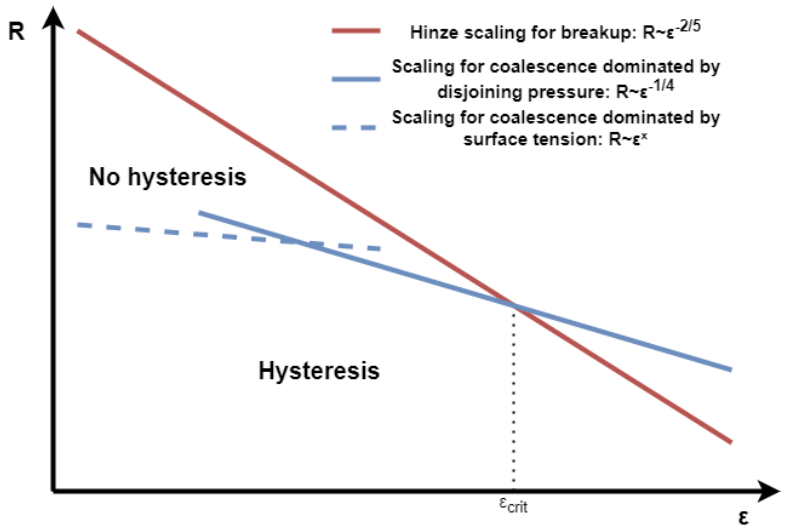

Figure 6.1: Sketch of the Hinze scaling and the scaling resulting from droplet coalescence. The dashed line indicates the scaling associated with droplet coalescence of highly deformable droplets, having a different slope than the case of non-deformable droplet. The existence of this scaling is not thought to have a significant effect on the emerging physics of hysteresis.

in figure 6.1. Hysteresis has been observed and studied extensively. However, whether it actually works the way illustrated by figure 6.1 is unknown. Therefore an important aspect of future research is finding the critical turbulent intensity for wide range of parameters.

Lastly, if the simulations of turbulent emulsions turn out to be successful, i.e. a critical turbulent intensity ε_{crit} is found, physical experiments could be performed to check whether this theory matches physical observations. This is an important step since a physical disjoining pressure by surfactants possibly behaves differently than the modelled disjoining pressure, e.g. when surfactant concentration changes due to changing surface area.

6.2 Remarks on performed numerical simulations

If doing more LBM droplet coalescence simulations, it is worth paying attention to some simulation related issues. First, the domain size: for most performed simulations two droplets with radius 40 were placed in a 256×256 fluid domain with periodic boundary conditions. This appears to be rather small, but using a 512×512 domain did not seem to yield a significantly different result. However, there is a more fundamental problem which are the boundary conditions: using solid walls or periodic boundary conditions (which are equivalent in symmetric flow) causes the surrounding fluid to flow around the droplet from the front to the back. This is an important difference with the physical situation, where surrounding fluid is moving along with moving droplets, which would be Stokes flow for a fully isolated droplet. The flow found in the current simulations is thought to only affect the flow of the surrounding fluid, however this surrounding fluid is having a major

influence on the droplet coalescence process e.g. by energy dissipation. The purpose here is not to argue that the current simulations are unreliable, but it is useful to investigate the influence of the following:

- Using a lower density for the surrounding fluid. The effect of the flow around the droplet is minimised, and thus also energy dissipation is lowered. On the other hand, hydrodynamical effects are reduced as well, probably resulting is less droplet deformation.
- Using open inflow or pressure boundary conditions, which will give insight in the effect of the boundary conditions on the flow around the moving droplets.
- Improving the stability of the Lattice Boltzmann Method using a Central Moments implementation [7]. Better stability allows using a lower viscosity and consequently reducing energy dissipation but keeping hydrodynamical effects by the surrounding fluid.

Being able to reduce energy dissipation would make obtaining data from the numerical simulations more straightforward. In section 3.2.2 the method was described to correct for high energy dissipation, which works surprisingly well but is still rather crude. Results without the necessity to correct, would be more convincing.

Besides the discussed issues with surrounding fluid flow and associated energy dissipation, more parameters of the simulations can be tuned. Now, the minimum range that was used is $\delta = 8$ and these results already appear to be somewhat inaccurate. To more convincingly verify the dependency on δ, more, thus higher, values should be checked. However, note that physically $\delta \ll R$ which is definitely not the case for $\delta = 32$ and $R = 40$ for example. A simple solution is increasing both the droplet size and the repulsion force range. It is not expected to obtain completely different results, however it can definitely have an effect on the additional contact area which was found but later neglected in the current work.

One last remark about the repulsion force range is that the ratio between the initial separation distance d and δ is also important. Ideally $\delta \ll d$ since the droplet should not be able to interact already at the beginning of the simulation. Increasing δ implies having to increase d on its turn resulting in higher energy dissipation since the droplets have to travel a further distance. A more fundamental point is that d was equal for all simulation, being equal to 15 lattice nodes. Varying this distance d could reveal any unwanted dependency on this arbitrary initial separation.

Then, recall the inaccurate results for using a high surface tension ($\sigma = 0.1$). This inaccuracy is thought to originate from droplet oscillation. Actually, oscillation of the droplets is undesirable since it is an artifact of the initialisation by the body force.

As discussed in section 4.2.1 also the disjoining pressure has boundaries for which values can be used, the values which are used are chosen based on practical feasibility. Too low disjoining pressure, implying low velocity causes the droplets to come to rest before coalescing. On the other hand, too high disjoining pressure causes the droplets to break instead of coalescing. For the simulations, these boundaries pose no problems since within these boundaries the disjoining pressure could be varied over multiple orders of magnitude. It is interesting to put the values in context by translating to physical values. The values of the dimensionless disjoining pressure used roughly range from 1×10^{-3} to 1. A typical water-oil surface tension is in the order of $1 \times 10^{-2}\,\mathrm{N\,m^{-1}}$, droplet size in emulsions is in the order of $1 \times 10^{-6}\,\mathrm{mm}$ and a typical disjoining pressure by surfactants on a water-oil interface is between 50 and 2000 Pa. For this parameters $\tilde{\Pi}$ lies between 5×10^{-3} and 2×10^{-1}, being just too low for having collisions with significant droplet deformation. However, it is possible easy to choose two fluids with a lower surface tension, inherently increasing $\tilde{\Pi}$.

Now let us have a look at the Weber number associated with critical droplet coalescence. For a dimensionless disjoining pressure in the range 5×10^{-3} - 2×10^{-1}, the Weber number approximately is in the range 5×10^{-4} - 5×10^{-2}. Using a fluid density of $1 \times 10^{3}\,\mathrm{kg\,m^{-3}}$ and the same droplet radius and surface tension as before we calculate that the typical droplet velocity is in the range 2 - $2 \times 10^{1}\,\mathrm{m\,s^{-1}}$. We conclude that the range used for the simulations is reasonably achievable in practice.

Bibliography

[1] D. Arumuga Perumal and Anoop K. Dass. A review on the development of lattice boltzmann computation of macro fluid flows and heat transfer. *Alexandria Engineering Journal*, 54(4):955–971, 2015. 13

[2] R. Aveyard, B. P. Binks, W.-G. Cho, L. R. Fisher, P. D. I. Fletcher, and F. Klinkhammer. Investigation of the forcedistance relationship for a small liquid drop approaching a liquidliquid interface. *Langmuir*, 12(26):6561–6569, 1996. 8

[3] Vance Bergeron. Forces and structure in thin liquid soap films. *Journal of Physics: Condensed Matter*, 11(19):R215–R238, jan 1999. 8

[4] P. L. Bhatnagar, E. P. Gross, and M. Krook. A model for collision processes in gases. i. small amplitude processes in charged and neutral one-component systems. *Phys. Rev.*, 94:511–525, May 1954. 12

[5] John A. Boxall, Carolyn A. Koh, E. Dendy Sloan, Amadeu K. Sum, and David T. Wu. Droplet size scaling of waterinoil emulsions under turbulent flow. *Langmuir*, 28(1):104–110, 2012. 4

[6] Shiyi Chen and Gary D. Doolen. Lattice boltzmann method for fluid flows. *Annual Review of Fluid Mechanics*, 30(1):329–364, 1998. 13

[7] Alessandro De Rosis, Rongzong Huang, and Christophe Coreixas. Universal formulation of central-moments-based lattice boltzmann method with external forcing for the simulation of multiphysics phenomena. *Physics of Fluids*, 31(11):117102, Nov 2019. 46

[8] Gregory Falkovich and Katepalli Sreenivasan. Lessons from hydrodynamic turbulence. *Physics Today*, 59(4):43, 2006. 4

[9] H. Feng. *Understanding and manipulating coalescence in dense emulsions*. PhD thesis, Wageningen University, 2013. WU thesis 5660. 8, 9

[10] Ivan Girotto. *Physics of Dense Emulsions via High-Performance Fully Resolved Simulations*. PhD thesis, Applied Physics, University of Modena and Reggio Emilia, July 2021. Proefschrift. 11

[11] Ivan Girotto, Karun P.N. Datadien, Gianluca Di Staso, and Federico Toschi. The chaotic life of mayonnaise, November 2019. 72nd Annual Meeting of the APS Division of Fluid Dynamics (DFD 2019) ; Conference date: 23-11-2019 Through 26-11-2019. 5

[12] M. Guskova, V. Shchur, and L. Shchur. Simulation of drop oscillation using the lattice boltzmann method. *Lobachevskii J Math*, 41:992–995, 2020. 32

[13] J.O. Hinze. Fundamentals of the hydrodynamic mechanism of splitting in dispersion processes. *AIChE Journal*, 1(3):289–295, 1955. 4, 7

[14] T. Kolarov, R. Cohen, and D. Exerowa. Direct measurement of disjoining pressure in black foam films ii. films from nonionic surfactants. *Colloids and Surfaces*, 42(1):49–57, 1989. 5

[15] A. N. Kolmogorov. A refinement of previous hypotheses concerning the local structure of turbulence in a viscous incompressible fluid at high reynolds number. *Journal of Fluid Mechanics*, 13(1):82–85, 1962. 7

[16] A.N. Kolmogorov. Dissipation of energy in the locally isotropic turbulence. *Dokl. Akad. Nauk. SSSR*, 32(1):15–17, 1941. 4, 6

[17] Ankit Kumar, Shigeng Li, Chieh-Min Cheng, and Deayeon Lee. Recent developments in phase inversion emulsification. *Ind. Eng. Chem. Res.*, 54(34):8375–8396, 2015. 4

[18] Nick Laan, Karla G. de Bruin, Denis Bartolo, Christophe Josserand, and Daniel Bonn. Maximum diameter of impacting liquid droplets. *Phys. Rev. Applied*, 2:044018, Oct 2014. 27

[19] Haihu Liu, Albert Valocchi, and Qinjun Kang. Three-dimensional lattice boltzmann model for immiscible two-phase flow simulations. *Physical Review E*, 85, 04 2012. 14

[20] David Julian Mcclements. Critical review of techniques and methodologies for characterization of emulsion stability. *Critical Reviews in Food Science and Nutrition*, 47(7):611–649, 2007. PMID: 17943495. 4

[21] A. Montessori, M. Lauricella, N. Tirelli, and S. Succi. Mesoscale modelling of near-contact interactions for complex flowing interfaces. *Journal of Fluid Mechanics*, 872:327–347, Jun 2019. 15

[22] Prasad Perlekar, Luca Biferale, Mauro Sbragaglia, S. Srivastava, and Federico Toschi. Droplet size distribution in homogeneous isotropic turbulence. *Physics of Fluids*, 24, 12 2011. 4

[23] H.M Princen. Rheology of foams and highly concentrated emulsions. ii. experimental study of the yield stress and wall effects for concentrated oil-in-water emulsions. *Journal of Colloid and Interface Science*, 105(1):150–171, 1985. 5

[24] Y. H Qian, D D'Humières, and P Lallemand. Lattice BGK models for navier-stokes equation. *Europhysics Letters (EPL)*, 17(6):479–484, feb 1992. 13

[25] R.M.S. Rosa. Turbulence theories. In Jean-Pierre Françoise, Gregory L. Naber, and Tsou Sheung Tsun, editors, *Encyclopedia of Mathematical Physics*, pages 295–303. Academic Press, Oxford, 2006. 7

[26] Cosima Stubenrauch and Regine von Klitzing. Disjoining pressure in thin liquid foam and emulsion films—new concepts and perspectives. *Journal of Physics: Condensed Matter*, 15(27):R1197–R1232, jun 2003. 8

[27] S.F. Wong, J.S. Lim, and S.S. Dol. Crude oil emulsion: A review on formation, classification and stability of water-in-oil emulsions. *Journal of Petroleum Science and Engineering*, 135:498–504, 2015. 4

[28] Lei Yi, Federico Toschi, and Chao Sun. Global and local statistics in turbulent emulsions. *Journal of Fluid Mechanics*, 912:A13, 2021. 4

[29] Yosang Yoon, Fabio Baldessari, Hector D. Ceniceros, and L. Gary Leal. Coalescence of two equal-sized deformable drops in an axisymmetric flow. *Physics of Fluids*, 19(10):102102, 2007. 9, 39

Appendix A

Derivations in three dimensions

Most derivations presented are almost fully the same in two and three dimensions. For completeness, all derivations are given below in 3D.

A.1 Repulsion energy

For the contact area A, we use the result of the two-dimensional case being $A \sim \sqrt{R\delta}$. Noting that the droplets are spherically symmetric, we simply square this expression to yield the contact area in three dimensions:

$$A \sim R\delta \tag{A.1}$$

Using the assumption for additional surface area presented in section 4.1.2 being $\frac{R-R_0}{R} \sim We^{1/2}$, we see that additional surface area scales as $\sim We$:

$$A \sim R\delta + cR^2\ We \tag{A.2}$$

Finalising the derivation with calculating the repulsion energy:

$$\begin{aligned} E_{rep} &\sim \Pi \left(R\delta + cR^2\ We\right) \delta \\ &= \Pi R^2 \delta \left(\frac{\delta}{R} + c\ We\right) \\ &= R\delta\sigma \left(\frac{\delta}{R} + c\ We\right) \tilde{\Pi} \end{aligned} \tag{A.3}$$

A.2 Surface energy

Assuming a conversion from kinetic energy to surface energy:

$$\begin{aligned} E_{kin} &\sim \Delta E_{surf} \\ \rho R_0^3 v^2 &\sim \Delta E_{surf} \\ \Delta E_{surf} &\sim \sigma R_0^2 \, We \end{aligned} \tag{A.4}$$

A.3 Criterion for droplet coalescence

Using equations (A.3) and (A.4) and assuming $E_{diss} = 0$, the energy balance, equation (4.1) is filled in:

$$\begin{aligned} \rho R^3 v^2 &= c_1 R \delta \sigma \left(\frac{\delta}{R} + c \, We \right) \tilde{\Pi} + c_2 \sigma R^2 \, We \\ \rho R v^2 &= c_1 \frac{\delta}{R} \sigma \left(\frac{\delta}{R} + c \, We \right) \tilde{\Pi} + c_2 \sigma \, We \\ We &= c_1 \frac{\delta}{R} \left(\frac{\delta}{R} + c \, We \right) \tilde{\Pi} + c_2 \, We \end{aligned}$$

As before writing as an expression for the dimensionless disjoining pressure, and assuming small Weber number:

$$\begin{aligned} c_1 \frac{\delta}{R} \tilde{\Pi} &= (\, We - c_2 \, We) \, / \left(\frac{\delta}{R} + c \, We \right) \\ c_1 \left(\frac{\delta}{R} \right)^2 \tilde{\Pi} &= (1 - c_2) \, We \end{aligned} \tag{A.5}$$

Based on the results presented in section 4.2.3 there are strong indications that also in three dimensions the assumed $\sim We$ scaling will not hold for the change in surface energy. On the other hand, there is no indication either that the scaling is the same as in two dimensions, i.e. $\sim We^{4/3}$. Therefore, we will use the assumption that the surface energy scales as some power γ of the Weber number: $\Delta E_{surf} \sim \sigma R^2 \, We^{\gamma}$. This results in the final equation:

$$c_1 \left(\frac{\delta}{R} \right)^2 \tilde{\Pi} = We - c_2 \, We^{\gamma} \tag{A.6}$$